

phenofit: An R package for extracting vegetation phenology from time series remote sensing

Dongdong Kong^{1,2}  | Tim R. McVicar³  | Mingzhong Xiao⁴  | Yongqiang Zhang⁵  | Jorge L. Peña-Arcibia³  | Gianluca Filippa⁶  | Yuxuan Xie¹ | Xihui Gu^{1,2} 

¹Department of Atmospheric Science, School of Environmental Studies, China University of Geosciences, Wuhan, China

²Centre for Severe Weather and Climate and Hydro-Geological Hazards, Wuhan, China

³CSIRO Land and Water, Black Mountain Science and Innovation Park, Canberra, Australia

⁴Center of Water Resources and Environment, School of Civil Engineering, Sun Yat-Sen University, Guangzhou, China

⁵Key Lab of Water Cycle and Related Land Surface Processes, Institute of Geographic Sciences and Natural Resources Research, Chinese Academy of Sciences, Beijing, China

⁶Climate Change Unit, Environmental Protection Agency of Aosta Valley, Valle d'Aosta, Italy

Correspondence

Mingzhong Xiao
 Email: xmingzh@mail2.sysu.edu.cn

Xihui Gu
 Email: guxh@cug.edu.cn

Funding information

Central Universities, China University of Geosciences (Wuhan), Grant/Award Number: CUG2106107; National Natural Science Foundation of China, Grant/Award Number: 4210011820

Handling Editor: Hooman Latifi

Abstract

1. Satellite-derived vegetation indices (VIs) provide a way to analyse vegetation phenology over decades globally. However, these data are often contaminated by different kinds of optical noise (e.g. cloud, cloud shadow, snow, aerosol), making accurate phenology extraction challenging.
2. We present an open-source state-of-the-art *R* package called *phenofit* to extract vegetation phenological information from satellite-derived VIs. *phenofit* adopts state-of-the-art phenology extraction methods, such as a weight updating function for reducing optical noise contamination, a growing season division function for separating the VI time series into different vegetation cycles, and rough and fine fitting functions for reconstructing VI time series. They work together to make phenology extraction from frequently contaminated VIs easier and more accurate.
3. Compared against other widely used phenology extraction tools, for example, TIMESAT and *phenopix*, *phenofit* provides flexible input and output options, a practical growing season division function, rich curve fitting and phenology extraction functions, and robust performance under different kinds of optical noise.
4. In addition to working with VIs from mesoscale satellites (e.g. MODIS and AVHRR), *phenofit* can also reconstruct vegetation time series and extract phenology using other sources, such as VIs from high-resolution optical satellites (e.g. Sentinel-2 and Landsat) and radar satellites (e.g. Sentinel-1), vegetation greenness indices from digital cameras and gross primary production estimations from eddy-covariance sites. As such, *phenofit* can contribute to the study of ecological process dynamics and assist in effective modelling of global change impacts on vegetation, as caused by climate variability and human intervention. Code and

data of case studies are available at <https://zenodo.org/record/6425745> (Kong, 2022a).

KEY WORDS

cloud contamination, R language, satellite data, time series reconstruction, vegetation indices, vegetation phenology

1 | INTRODUCTION

Vegetation phenology is the study of recurring patterns of plant growth and development, for example, the time of (a) budburst, (b) plant flowering, (c) leaf greenup and (d) senescence (Lieth, 1974). It has been widely accepted that vegetation phenology is a key indicator of global climate change, which is strongly connected with warming temperatures (Joiner et al., 2018; Peñuelas & Filella, 2001; Piao et al., 2019; Zhang et al., 2018). It is a key component of the Earth system, providing feedback to the local environment and regional climate systems by altering foliage coverage, surface roughness length, albedo, emissivity and transpiration (Hufkens et al., 2018; Kong et al., 2020; Peñuelas et al., 2009; Richardson et al., 2013; Miaogen Shen et al., 2015), which impacts the carbon, water and energy cycles (Barichivich et al., 2013; Lian et al., 2020; Piao et al., 2007; Torre Cerro & Holloway, 2021). Therefore, monitoring vegetation phenology is vital for understanding the mutual feedback between vegetation dynamics and climate change.

Satellite-derived vegetation indices (VIs) provide an opportunity to monitor vegetation phenology over decades globally. Derived phenological metrics, such as the start and end of the growing season, are important to assess vegetation condition and vegetation response to climate change (Dong et al., 2019; Fensholt et al., 2015; Harwood et al., 2016; Lambin, 1999; Lausch et al., 2018; Whitcraft et al., 2019). However, it is still challenging to extract vegetation phenology from satellite-derived VIs as they are frequently contaminated by, *inter alia*, cloud, cloud shadow, snow, aerosol (Kong et al., 2019; Wilson & Jetz, 2016). For example, the analysis of the 16-day composited Moderate Resolution Imaging Spectroradiometer (MODIS) Enhanced Vegetation Index (EVI) over land (excluding Antarctica and Greenland) during 2000–2017 showed that, at a global level, only 44% of the observations were uncontaminated (Figure S1). When contaminated, satellite-derived VIs are usually underestimated (Holben, 1986) and become unreliable (Cihlar et al., 1997; Hilker et al., 2012; Xiao et al., 2003). Inappropriate processing of contaminated VI points in the time series phenology analysis can lead to a systematic bias, partly obscuring the real signal of biophysical change, and so resulting in erroneous phenological metrics (Shen et al., 2013; Yang et al., 2015).

Phenology extraction from satellite-derived VIs is built upon the following three steps: (a) division of time series into shorter sequences, each representing a vegetation growing season (herein denoted as ‘growing season division’); (b) curve fitting (also known as VI time series reconstruction) and (c) phenological metrics extraction. To our knowledge, TIMESAT is the only software that

combines all of the above three steps (Jönsson & Eklundh, 2002; Jönsson & Eklundh, 2004). After the initial release of TIMESAT in 2002 (Jönsson & Eklundh, 2002), many researchers have sought to improve vegetation phenology extraction (Alleaume et al., 2018; Beck et al., 2006; Chen et al., 2004; Elmore et al., 2012; Gu et al., 2009; Kong et al., 2020; Moussus et al., 2010; Zhang, 2015; Zhang et al., 2004). But much of their work only focused on one or two parts of the above phenology extraction steps. A comprehensive software that combines all of their contributions and provides flexible options in phenology extraction is still lacking.

Phenology extraction software has been routinely used since the early 2000s. Examples of this are, as mentioned before, TIMESAT (Jönsson & Eklundh, 2002), *greenbrown* (Forkel et al., 2015) and *phenopix* (Filippa et al., 2016) (Table 1). TIMESAT is one of the most widely used phenology extraction software (Jönsson & Eklundh, 2002; Jönsson & Eklundh, 2004; Palmer et al., 2015; Tan et al., 2011). However, being not open source, it is difficult to incorporate newly proposed curve fitting methods [e.g. Beck logistic (Beck et al., 2006)] and Elmore logistic (Elmore et al., 2012)] and phenology extraction methods [e.g. inflection method (Zhang et al., 2003) and Gu method (Gu et al., 2009)]. *phenopix* is another well-known phenology extraction software in R language (Filippa et al., 2016), which inherits much of the underpinning logic from *greenbrown* (Forkel et al., 2015), yet *phenopix* is mainly designed for high-frequency ground-based digital camera greenness time series (Richardson et al., 2018), and has no function to handle contaminated points common in time series satellite-derived VIs (Coluzzi et al., 2018; Kong et al., 2019).

In this study, we present and evaluate an open-source state-of-the-art vegetation phenology extraction package coded in R language, called *phenofit*. Herein *phenofit* is written all in italic lower case font to distinguish it from Chuine and Beaubien’s (2001) ‘weather-driver phenological response’ model called PHENOFIT (all capitals and non-italic). *phenofit* combines all state-of-the-art growing season division, curve fitting and phenology extraction methods, and provides flexible input and output routines, making phenology extraction more accurate and easier to implement.

2 | PHENOFIT R PACKAGE

phenofit was designed on the principles of universal applicability, ease of use and ease of extending to incorporate different methods: a. *phenofit* minimizes the influence of contamination (e.g. cloud, cloud shadow, snow, aerosol);

TABLE 1 Comparison of *phenofit* with TIMESAT and *phenopix* (✓: Supported, ✗: Non-supported)

Module	Details	<i>phenofit</i>	TIMESAT	<i>phenopix</i>
Input</annotation>	Missing values	✓	✓	✓
	Uneven step time series	✓	✗	✓
	Sites with different length	✓	✗	✓
	Multiple optical data sources	✓	✓	✗
	VIs instead of reflectance data	✓	✓	✗
Growing season division	Multiple growing seasons/year	✓	✓	✗
	Dynamic growing season	✓	✗	✗
Curve fitting	Parameters' boundary constraints	✓	✗	✗
	Weight updating	wTSM, wBisquare, wChen	wTSM	✗
Phenology Extraction	Phenology extraction method	TRS, DER, Inflection, Gu	TRS	TRS, DER, Inflection, Gu
Output	Time-scale of the reconstructed time series	User-specified	As the Input	User-specified
	Parameters of curve fitting functions	✓	✓	✓
	Direct date of phenological metrics	✓	✗	✓

- b. *phenofit* is suitable for regions where vegetation has multiple growing seasons in a year and/or land cover has changed (e.g. deforestation, reafforestation, bushfire and recovery);
- c. the input of *phenofit* is flexible and supports both evenly and unevenly spaced time series, and can handle missing input values;
- d. the output of *phenofit* is friendly and includes detailed information about growing season division, reconstructed daily time series, curve fitting parameters and extracted phenological metrics; and
- e. from a software development perspective, it is easy to extend

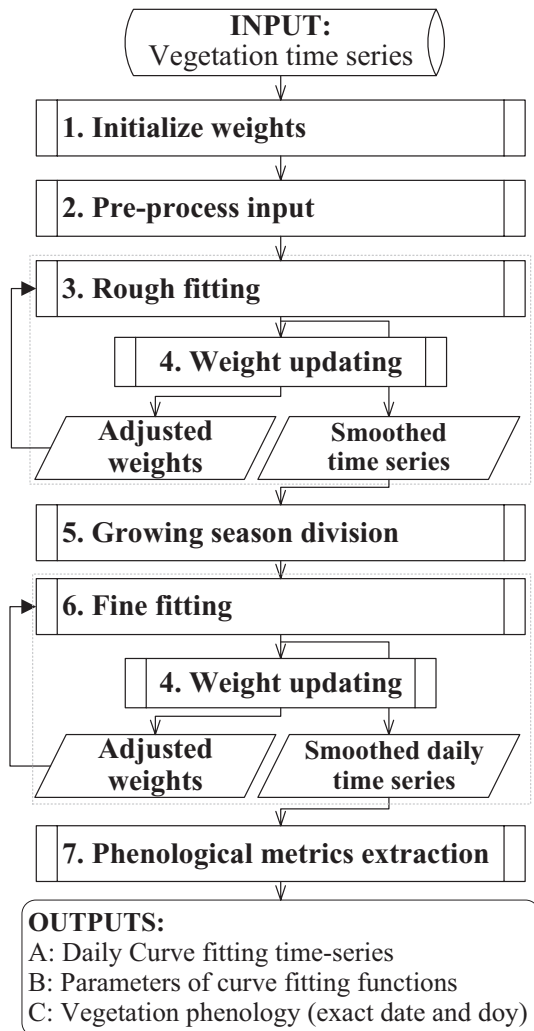


FIGURE 1 Flowchart of phenology extraction in *phenofit*. The steps numbered 1 to 7 correspond to the sub-headings of Section 2

phenofit by including newly developed methods. Functions of the same topic have a unified form, for example, same input parameters and same output structure. The workflow of *phenofit* is shown in Figure 1. Details are shown in the following sections.

2.1 | Initialize weights

VI time series reconstruction should mainly rely on information from good-quality points, but also extract the limited information available from the marginal- and bad-quality points. Depending on the situation, marginal- and bad-quality points may also contain valuable information. For example, snow-contaminated points can help to distinguish the end of growing season and the background VI value during the non-growing season (Shen et al., 2013; Zhang et al., 2006).

We initialize weights according to their Quality Control (QC) information (e.g. *SummaryQA* in MOD13A1, *StateQA* in MOD09A1).

VI observations are grouped into three categories, that is, good, marginal and bad, which have corresponding weights of maximum (w_{\max}), middle (w_{mid}) and minimum (w_{\min}), respectively. *phenofit* provides multiple initial weight functions for various satellite VIs products (<http://phenofit.top/reference/qcFUN.html>). For satellites or VIs that are not covered in *phenofit* (e.g. QA_pixel in Landsat 8 OLI/TIRS surface reflectance), users can group VI observations into those three categories and similarly initialize their weights. We know that the real VI values are usually larger than the contaminated remotely sensed observations (Holben, 1986; Zhang, 2015). This means that contaminated observations also can provide valuable information and w_{\min} should be greater than zero. If $w_{\min} = 0.0$ then 'bad' data points will be completely ignored. Generally, w_{\max} , w_{mid} and w_{\min} can be 1.0, 0.5 and 0.2 (Kong et al., 2019, 2020). For VIs time series without QC information, weights of all valid points are equally set to w_{\max} , and weights of missing values are set to w_{\min} . As missing values have no valuable information, in this instance w_{\min} can be set to 0.0.

In *phenofit*, rough fitting and fine fitting are solved similarly to weighted linear regression (Cleveland, 1979) by minimizing the cost function J (defined as weighted sum squared error), where weights play a regulatory role and exert impact directly on the results of rough fitting and fine fitting. J is described as:

$$J = \sum (y_i - \hat{y}_i)^2 w_i , \quad (1)$$

where the subscript i means the i th element; y is the original VI time series; \hat{y} is the result of rough fitting or fine fitting; and w is the weights in the curve fitting procedure.

2.2 | Pre-process input VI

The *check_input* function in *phenofit* is used to pre-process input VI in the following two aspects: (a) Discard spike values and missing values. A point is flagged as a 'spike' if the absolute difference of y_i and $y_{\text{mov},i}$ is greater than two times the standard deviation of the entire time series, where y_i is the i th observation of the input VI, and $y_{\text{mov},i}$ is the corresponding three-point moving average. As *phenofit* can deal with unevenly spaced series, spike values altogether with missing values are discarded. (b) Obtain lower and upper bounds (abbreviated as *ylu*) of VI time series according to good-quality observations (Kong et al., 2019), which are mainly used to constrain the value of contaminated VIs in a reasonable range, especially in the presence of a snowy non-growing season. Points beyond the range of *ylu* are regarded as suspicious, corresponding values and weights are reassigned to y_{\min} (lower bound in *ylu*) and w_{\min} respectively.

2.3 | Rough fitting

Rough fitting is used to capture vegetation seasonal signals, which is further utilized to divide vegetation growing seasons

FIGURE 2 Illustration of the growing season division method. GPP estimation at flux site 'IT-CA1' during Jan/2012-Dec/2014 was used here (<http://sites.fluxdata.org/IT-CA1/>). In the procedure of rough fitting, wWHIT is used. The horizontal red dot lines are lower and upper bounds (y_{lu}) defined in section 2.2. Later iterations are displayed 'on top' of earlier iterations

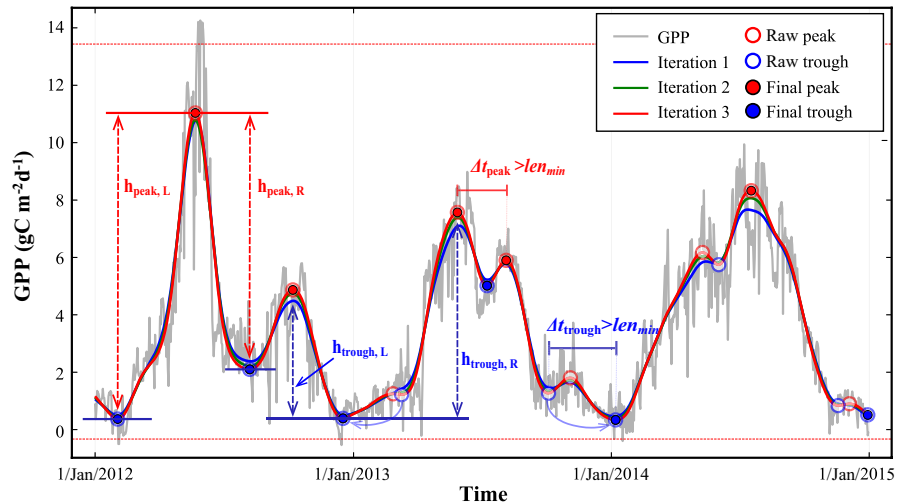


(Figure 2). Three rough fitting functions are available in *phenofit*: (a) weighted Savitzky–Golay (wSG); (b) weighted HANTS (wHANTS) and (c) weighted Whittaker (wWHIT) (Table 2). Previous studies have shown that not one of these three rough fitting functions always outperforms the others in all situations (Kong et al., 2019; Yang et al., 2015). Generally, wSG is optimal for vegetation that has experienced abrupt changes (e.g. clearing or bushfires, Cao et al., 2018; Chen et al., 2004); wHANTS is for vegetation that has a clear and stable growing season (Bush et al., 2017; Yang et al., 2015); wWHIT is for vegetation whose growing season changes dynamically (e.g. cropping in both good and drought years, Atzberger & Eilers, 2011; Kong et al., 2019). As shown in Kong et al. (2019) (their figure 8 and table 5), wWHIT is more robust for outliers than wSG and wHANTS, and can capture vegetation seasonal signals even when the input VI time series has more than 30% points contaminated. Hence, wWHIT is the default option for rough fitting in *phenofit*.

When using rough fitting, users should choose parameters carefully. *frame*, *nf* and λ are the most sensitive parameters of wSG, wHANTS and wWHIT, respectively. Based on previous studies (Kong et al., 2019, 2020), the optimal parameters of wSG and wWHIT are more stable than that of wHANTS. Generally, (a) *frame* can be *nptperyear**2/5 (*nptperyear* is the number of VI observations per year and per pixel, Eklundh & Jönsson, 2017); (b) *nf* depends on the number of seasons (*nseason*), and ideally should be an even multiple of *nseason* (i.e. $2 \times nseason \times m$, $m \in$ positive integer, Yang et al., 2015); and (c) λ depends on the time scale of input VI, and can be 10,000, 15 and 5, respectively, for daily, 8-day and 16-day input (Kong et al., 2019, 2020). Meanwhile, the V-curve theory for the automatic selection of Whittaker smoother's parameter λ is implemented for wWHIT in *phenofit* (Eilers et al., 2017; Frasso & Eilers, 2015; Kong et al., 2019). If set $\lambda = \text{NULL}$, V-curve theory will be employed automatically to determine the optimal λ , which makes wWHIT having a good balance between fidelity and roughness and benefits *phenofit* in vegetation seasonal signals reconstruction and growing season division.

2.4 | Weight updating

After each iteration of rough fitting or fine fitting (see Figure 1), a weight updating function is applied to adjust the weighting of each point in the time series. We know that points located above [below] the curve of rough or fine fitting, are underestimated [overestimated] in the curve fitting procedure. In the case of contaminated satellite-derived VIs, values are usually lower than normal (Holben, 1986). A relatively high value (underestimated point in the curve fitting procedure) is more likely to have a better quality than a low value (overestimated point). Hence, the weight updating function tends to (a) increase the weight of underestimated points and decrease the weight of overestimated points to minimize contamination effects and approach the upper envelope of VI time series and (b) decrease the weight of outliers to minimize their interference. Outliers in *phenofit* are defined in the same strategy of the *bisquare* function in robust regression (see details in Kong et al., 2019; their Equation 10).

Weight updating makes *phenofit* robust when capturing VI vegetation seasonal signals and reconstructing vegetation daily time series. Three weight updating functions are provided in *phenofit*, being (a) modified bisquare *wBisquare* (see Kong et al., 2019 for details); (b) weight updating of TIMESAT *wTSM* (Jönsson & Eklundh, 2002) and (c) weight updating of Chen et al. (2004) *wChen*. Due to the stable performance, *wBisquare* and *wTSM* are the suggested options (Jönsson & Eklundh, 2004; Kong et al., 2019).

2.5 | Growing season division

Growing season division is a crucial step in the procedure of phenology extraction. Implementing an inappropriate method, or just equating the growing season as the calendar year, can lead to completely wrong phenological metrics in regions that have multiple growing seasons in a calendar year (e.g. cropland and grassland; Luo et al., 2020) or growing seasons that straddle two

TABLE 2 Rough fitting functions available in *phenofit*. The star system rating for fidelity and smoothness is based on the *phenofit* developers' experience and results in Kong et al. (2019). Fidelity denotes the correspondence of the output signal to the input signal; smoothness denotes continuity without abrupt changes. Nf is the number of frequencies for *wHANTS*; frame is the moving window size of *wSG*; λ is the smoothness parameter of *wWHT*

Functions	Parameters	Fidelity	Smoothness	Advantage	Dissadvantage	References
<i>wHANTS</i>	<i>nf</i>	★★★	★★★★★	Good smoothness	Cannot capture rapid change Has an apparent shape of sine and cosine; sensitive to parameter <i>nf</i>	Verhoef (1996); Yang et al. (2015)
<i>wWHT</i>	λ	★★★★★	★★★★★	Good fidelity Good balance of fidelity and smoothness	Sensitive to regional fluctuations Low computational efficiency Cannot capture rapid change	Eilers (2003); Kong et al. (2019)

^aOf the two parameters in *wSG*, the parameter polynomial order (d) is less sensitive than the parameter windows size (frame); hence, we only describe the most sensitive parameter.

calendar years, for example, austral summer irrigated crops (Van Niel & McVicar, 2004) and boreal irrigated crops (Luo et al., 2020; Peña-Arancibia et al., 2021); Based on the idea that only one peak value is inside a growing season and two trough values define a growing season, we proposed a practical method to perform growing season division (Figure 2) encoded as the *season_mov* function within *phenofit*. This method has been successfully applied to MODIS Normalized Difference Vegetation Index (NDVI), EVI and Gross Primary Production (GPP) estimations on 95 flux tower sites, located across 10 IGBP (the International Geosphere-Biosphere Programme) vegetation classes from tropical to cold regions (Kong et al., 2020).

Growing season division requires that vegetation seasonal signals be accurately determined, and *phenofit* uses the complementary strengths of rough fitting and fine fitting to do this. Rough fitting captures vegetation's gradual signal and divides the VI time series into growing seasons, while fine fitting is used to reconstruct vegetation daily time series in every growing season. *phenofit*'s growing season division has been introduced previously (Kong et al., 2020; their Figure 2); the following description is derived from there with minor modifications. The method has the following steps:

- Rough fitting is applied to suppress abnormal fluctuations and retrieve the seasonal component. Through the weight updating function, rough fitting reduces the weights of outliers to minimize their influence and increases the weights of underestimated points to approach the upper envelope of the VI time series. The default number of iterations is three. But if users want to retain the signal of multiple seasons within a year, the number of iterations should be reduced to two or one. In the procedure of approaching the upper envelope, it will inevitably reduce, or even confound the seasonal signal. Hence, rough fitting should be applied in limited iterations.
- Using the final smoothed VI time series from the rough fitting, local maxima (minima) are detected and regarded as raw peaks (troughs).
- Subtle fluctuations in rough fitting curves might introduce fake growing season peaks and troughs. The following criteria are applied to identify the real ones:

- Real peaks should satisfy that $\max(h_{\text{peak,L}}, h_{\text{peak,R}})$ and $\min(h_{\text{peak,L}}, h_{\text{peak,R}})$ are greater than $r_{\max}A$ and $r_{\min}A$, respectively:

$$\begin{cases} h_{\text{peak,L}} = y_{\text{peak}} - y_{\text{trough,L}}, \\ h_{\text{peak,R}} = y_{\text{peak}} - y_{\text{trough,R}}, \end{cases}, \quad (2)$$

$$\begin{cases} \max(h_{\text{peak,L}}, h_{\text{peak,R}}) > r_{\max}A, \\ \min(h_{\text{peak,L}}, h_{\text{peak,R}}) > r_{\min}A, \end{cases}, \quad (3)$$

where $h_{\text{peak},L}$ and $h_{\text{peak},R}$ are the height difference from the growing season peak to the left-hand and right-hand troughs, respectively (see Figure 2); A is the amplitude of the input time series y ; r_{\max} and r_{\min} are user-defined threshold parameters. Heuristic testing revealed that relatively small thresholds, $r_{\max} = 0.2$ and $r_{\min} = 0.05$, can eliminate most unrealistic peaks. Whereas using larger thresholds might mask real growing season peaks. The amplitude of the real growing season VI should have a considerable magnitude, and the magnitude of the left side and right side (i.e. $h_{\text{peak},L}$ and $h_{\text{peak},R}$) are likely different (McVicar & Jupp, 1998). Taking the year 2013 in Figure 2 as an example, two growing seasons exist in 2013. The gap between the first and second growing seasons is short (69 days), where $h_{\text{peak},R}$ of the first season and $h_{\text{peak},L}$ of the second season are quite small (being 0.88 and 0.53 gC m⁻² d⁻¹, respectively). That situation is quite common in double growing season systems (e.g. rotation of winter wheat and summer maize, Luo et al., 2020). Hence, $\max(h_{\text{peak},L}, h_{\text{peak},R})$ and $\min(h_{\text{peak},L}, h_{\text{peak},R})$ should be constrained by different thresholds ($r_{\max}A$ and $r_{\min}A$ respectively) to avoid eliminating real peaks.

1. The real troughs should satisfy that $\max(h_{\text{trough},L}, h_{\text{trough},R})$ is greater than $r_{\max}A$:

$$\begin{cases} h_{\text{trough},L} = -(y_{\text{trough}} - y_{\text{peak},L}), \\ h_{\text{trough},R} = -(y_{\text{trough}} - y_{\text{peak},R}), \end{cases} \quad (4)$$

$$\max(h_{\text{trough},L}, h_{\text{trough},R}) > r_{\max}A, \quad (5)$$

where $h_{\text{trough},L}$ and $h_{\text{trough},R}$ are the height difference of trough to the left-side and right-side peaks, respectively, Figure 2. Because the VI time series are stable in the non-growing season where $\min(h_{\text{trough},L}, h_{\text{trough},R})$ approaches zero, we do not constrain $\min(h_{\text{trough},L}, h_{\text{trough},R})$.

TABLE 3 Fine curve fitting functions available in the *phenofit* R package. T is the corresponding date of y (e.g. time series of VI); mn and mx are the minimum and maximum value of y ; sos and eos , respectively, denote the start of the growing season and end of the growing season; rsp and rau are, respectively, the rate of spring Greenup and autumn senescence; t_0 is the turning point of vegetation Greenup and senescence; $a3$ and $a5$ are the shape parameters of AG; m_7 is the summer greendown parameter; $c1$ and $c2$ are the shape parameters of Gu logistic

Function		Name	References
FitAG	$f(t) = \begin{cases} \frac{mx-mn}{e^{(rsp(t-t_0))^a3}} + mn, & t \leq t_0 \\ \frac{mx-mn}{e^{(rau(t-t_0))^a5}} + mn, & t > t_0 \end{cases}$	AG	Jönsson and Eklundh (2004)
FitDL.Zhang	$f(t) = \begin{cases} \frac{mx-mn}{1+e^{-rsp(t-sos)}} + mn, & t \leq t_0 \\ \frac{mx-mn}{1+e^{-rau(t-eos)}} + mn, & t > t_0 \end{cases}$	Zhang	Zhang et al. (2003)
FitDL.Beck	$f(t) = mn + (mx - mn) \cdot \left(\frac{1}{1+e^{-(rsp(t-sos))}} + \frac{1}{1+e^{(rau(t-eos))}} - 1 \right)$	Beck	Beck et al. (2006)
FitDL.Elmore	$f(t) = mn + (mx - m_7t) \cdot \left(\frac{1}{1+e^{-rsp(t-sos)}} - \frac{1}{1+e^{-rau(t-eos)}} \right)$	Elmore	Elmore et al. (2012)
FitDL.GU	$f(t) = mn + \frac{a_1}{[1+e^{-rsp(t-sos)}]^{c_1}} - \frac{a_2}{[1+e^{-rau(t-eos)}]^{c_2}}$	Gu	Gu et al. (2009)

1. The time lag of the two nearest peaks (and troughs) should be at least longer than len_{\min} (1.5~4 months should be a good choice; the default is 1.5 months in *phenofit*).

Raw peaks and troughs which cannot meet the above criteria are removed. After this step, if two troughs (or peaks) are next to each other, only the minimum (or maximum) one remains, for example, the fake trough in 2013 and the fake peak in 2014 are removed in Figure 2.

Finally, two troughs define a growing season. Growing season ID is defined as year_k to distinguish growing seasons; where year is the year where the peak is located, k is the order of growing seasons in this year. The first season in the year is corresponding to $k = 1$. To avoid confusion with phenological metrics defined in Section 2.7, the start [end] of growing season division is named as division start [end].

2.6 | Fine fitting

Fine fitting is used to capture vegetation's rapid changes in every growing season. Currently, five fine curve fitting methods are provided in *phenofit* to reconstruct daily VI time series (Table 3). Their equations differ in the number of parameters and hence distinguish their flexibility. The performance of those curve fitting methods has been evaluated at 95 flux sites in Kong et al. (2020). Asymmetric Gaussian (AG) fit has a similar form and performance as piecewise logistics fit (Zhang et al., 2003; abbreviated as Zhang hereafter). For AG and Zhang, being piecewise functions, the middle of the growing season sometimes is not continuous and less smooth than Beck and Elmore logistics. Beck, Elmore, and Gu logistics have a more stable and satisfactory performance than AG and Zhang (Kong et al., 2020; their Section 4.1). But due to using many parameters, the computing efficiency of Gu logistic is the lowest among the five methods. Therefore, Beck and Elmore are the suggested options.

The performance of fine fitting directly determines the accuracy of extracted phenological metrics. *phenofit* uses the following two

strategies to promote the performance of fine fitting. First, *phenofit* constrains fine fitting parameter boundaries according to their ecological meaning (Table 4), so parameters have a reasonable range and converge quickly. These parameter bounds are relatively broad, which suits most cases. Second, for every growing season, the previous and subsequent nextend good-quality observations also participate in the fine fitting procedure (Zhang, 2015; Zhang et al., 2007); this ensures the reconstructed time series is smoothly connected across different growing seasons.

2.7 | Phenological metrics extraction

The reconstructed daily scale time series from fine fitting is used to extract phenological metrics from every growing season. Four widely used phenology extraction approaches are provided in *phenofit* (Figure 3), these are as follows: (a) threshold method (TRS), (b) derivative method (DER), (c) inflection method (Klosterman et al., 2014; Zhang et al., 2003) and (d) Gu method (Filippa et al., 2016; Gu et al., 2009; Zhang et al., 2018). It should be noted that the inflection method is less stable than the others, as it requires VI time series having two local maxima and two local minima values of the change rate of curvature, but this situation cannot always be satisfied. Because phenological metrics defined by different methods have different ecological meanings, users should select phenology extraction methods according to the research purpose. Some guidelines can be found in Table 2 of Kong et al. (2020).

3 | DATA

To illustrate the performance of *phenofit*, we tested *phenofit* using the following data:

- (i) Test Data 1: Satellite-derived VI time series from a site with frequent contamination;

MOD13A1.006 EVI (<https://lpdaac.usgs.gov/products/mod13a1v006/>) is one of the most frequently used VI in the study of land surface vegetation dynamics (Huete et al., 2002; Kong et al., 2020; Zhang et al., 2017), with the spatiotemporal resolution of 500 m and 16 days (Didan et al., 2015). The MOD13A1.006 EVI data from the flux-tower site denoted CA-NS6 (<http://sites.fluxdata.org/CA-NS6/>) during 2010–2016 were used, which is located in a continental boreal forest at -98.9644°E , 55.9167°N , 244 m asl in Manitoba Province, Canada (Goulden, 2016; Wang et al., 2003). CA-NS6 was selected due to its representativeness of clear seasonality and frequent contaminations of snow and cloud. The clear seasonality helps *phenofit* focus on the evaluation of robustness to frequent contamination.

- (i) Test Data 2: Synthetic VI time series containing multiple growing seasons per year and changing land cover;

TABLE 4 Parameter boundaries of fine curve fitting functions in Table 3. pop denotes when the peak of (the growing) season occurred, y_{\min} (y_{\max}) is the minimum (maximum) value of vegetation time series y , rsp (rap) is the growing rate of spring and autumn, t_{\min} (t_{\max}) is when the growing season begins (ends), $k_0 = 4 / T_{\text{half}} * 2.67$ (see Supplementary Text 1 for the detailed deduction of k_0), $T_{\text{half}} = (t_{\max} - t_{\min}) / 2$, $A = y_{\max} - y_{\min}$, $\Delta y = 0.1A$ and $\Delta t = T_{\text{half}}/2$

Name	Lower	Upper	Description
t_0	$pop - \Delta t$	$pop + \Delta t$	Breakpoint of spring season and autumn season
mn	$y_{\min} - \Delta y$	$y_{\min} + \Delta y$	Background value
mx	$y_{\max} - \Delta y$	$y_{\max} + \Delta y$	Maximum value
sos	t_{\min}	$pop + \Delta t$	Start of growing season
eos	$pop - \Delta t$	t_{\max}	End of growing season
rsp	$k_0 / 3$	$3k_0$	Rate of spring greenup
rap	$k_0 / 3$	$3k_0$	Rate of autumn senescence

Spring shape parameter of FitAG

Autumn shape parameter of FitAG

Summer greendown parameter of FitDL

Elmore

Amplitude of spring season

Amplitude of autumn season

Spring shape parameter of FitDL

Gu

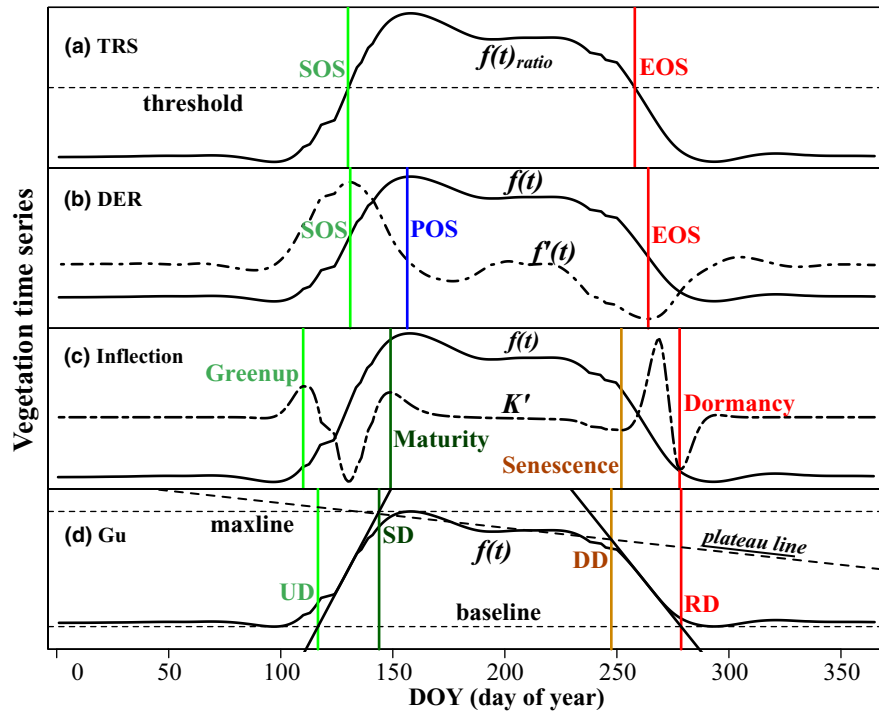


FIGURE 3 Schematic of the vegetation phenology extraction methods. This figure is modified from Filippa et al. (2016) with permission. (a) Threshold method (TRS): $f(t)$ is the original vegetation time series. $f(t)_{ratio} = (f(t) - \text{max}) / (\text{max} - \text{min})$, is the normalized vegetation time series in the range of [0, 1], as is the threshold. Start of growing season (SOS) and end of growing season (EOS) are defined as the first day when the VI value exceeds and subceeds the threshold, respectively. (b) Derivative method (DER): $f(t)'$ is the first-order derivative of $f(t)$. SOS (EOS) is the day with the fastest growing (senescence) rate. The peak of season (POS) is the position of the $f(t)$ maximum. (c) Inflection method (Zhang et al., 2003): K' is the change rate of curvature (Klosterman et al., 2014; Zhang et al., 2003); two local maxima of the change rate of curvature K' define Greenup and Maturity; two local minima of K' defines Senescence and Dormancy (Zhang et al., 2003). (d) Gu method (Gu et al., 2009): baseline and maxline correspond to the lower and upper boundary of $f(t)$. The maximum and minimum of $f(t)'$ defines slope of two tangent lines (recovery line and senescence line) to $f(t)$. The intersections of recovery and senescence lines with baseline and maxline define four phenological metrics: update date (UD), stabilization date (SD), initial downturn date (DD_0) and recession date (RD). To consider middle season greendown, defines a plateau line that linear fits to VI time series between SD and DD_0 . The intersection of plateau line with senescence line defines the final adjusted downturn date (DD) which is shown on (d) with DD_0 not being presented

We produced a synthetic VI time series with multiple growing seasons and changing land cover to test the performance of *phenofit*'s growing season division in a complex vegetation system. The Beck logistic method was chosen due to its parsimony in parameters (Table 3). The synthesized VI time series have 6 years covering 2010–2015, with a temporal resolution of 8-day (namely 46 observations per year). The first 2 years (i.e. 2010 and 2011) have one growing season each, then the second 2 years (i.e. 2012 and 2013) have two growing seasons each, with the third 2 years (i.e. 2014 and 2015) having a triple growing season each year. Changes in growing seasons reflect changes in land cover. We also simulated Gaussian noise with the same length as the VI time series to represent the interference of cloud, which belongs to a normal distribution with the mean and standard deviation of 0.0 and 0.05, respectively. We replaced the positive noise with zero and only retained the negative noise because cloud contaminated VIs are generally lower than the non-cloud contaminated VIs (for the same vegetation/land cover type; Holben, 1986; Zhang, 2015). Finally, the simulated noise was added to the synthesized VI time series. The

detailed information (e.g. *sos*, *eos*, *rsp* and *rau* of each growing season) is shown in Table S1.

- (i) Test Data 3: Observed eddy-covariance GPP time series, from 9 FLUXNET2015 sites containing multiple growing seasons per year.

FLUXNET2015 dataset provides long-term biological measurements globally across various climate and land cover types (Pastorello et al., 2020), which has been frequently used in various ecophysiology studies. As phenology extraction is the most challenging question in regions with multiple growing seasons, sites with multiple growing seasons from the FLUXNET2015 tier1 dataset (<https://fluxnet.org/data/fluxnet2015-dataset>) were selected to assess the performance of *phenofit* using the GPP data. The night-time partitioned daily-scale GPP estimations were used. Site-years with valid GPP estimations <70% were removed (Kong et al., 2020). Finally, 9 flux sites (Table S2) containing 73 site-years were selected.

4 | PHENOFIT'S USAGE AND PERFORMANCE

4.1 | Application to site scale

We illustrate the basic usage of *phenofit* using the previously described Test Data 1 (Section 3.1). To extract vegetation phenology with *phenofit*, VI time series (y), corresponding observed date (t), and weights (w , initialized by *qcFUN*) are required. There are four functions that *phenofit* calls in sequence: (a) *check_input*, (b) *season_mov*, (c) *curvefits* and (d) *get_pheno*. The function *check_input* is used to pre-process the input VI time series; *season_mov* conducts the rough fitting and performs growing season division; *curvefits* implements the fine fitting and reconstructs the daily VI time series in every growing season; finally *get_pheno* extracts the vegetation phenological metrics from the reconstructed daily VI time series. Detailed documentation for these four functions is available at <http://phenofit.top/reference/index.html>.

Figure 4 exhibits the results of rough fitting and growing season division returned by the function *season_mov* at Test Data 1, where the rough fitting function *wWHIT* was used due to its robust performance (Kong et al., 2019). It can be seen that: *ylu* helps to filter outliers in the non-growing season and contributes to more reasonable background values (i.e. VI values in the non-growing season). Additionally, the weight updating function and initial weights make *phenofit* minimize the influence of outliers in the growing season, for example, the abnormally high value flagged with 'marginal' at the end of 2015 (Figure 4). Those two factors help the rough fitting function encoded in *season_mov*, robustly capture the vegetation seasonal signal. The rough fitting result was further passed to the growing season division module (also implemented in *season_mov*). Test Data 1 has a clear seasonal signal and *phenofit* divides growing seasons correctly (Figure 4). The robustness of growing season division with complex time series was further evaluated based on Test Data 2 and 3 in Sections 4.3 and 4.4.

After rough fitting and growing season division, fine fitting was applied in every growing season to reconstruct vegetation daily time series. Figure 5 shows the fine fitting results of AG, Beck, Elmore, Gu and Zhang methods at CA-NS6. Due to its inherent property, fine fitting is superior to rough fitting to capture rapid changes of vegetation greenness, especially at the start and end of the growing seasons (Figure 5). Fine fitting avoids the unreasonable fluctuations that rough fitting can suffer from, for example at the end of the 2015 growing season (Figure 4). The parameter boundary constraints further contribute to the stable performance of fine fitting. Without it, fine fitting can be easily non-convergent (e.g. AG fine fitting in Figure S2) and phenological meaning will be lost (Table S3a). Taking Elmore double logistics as an example, when parameters are constrained with the values provided in Table 4, the range of parameter *rsp* (rate of spring greenup) is 0.08–0.19 (in EVI units/day) over 2010–2016. In comparison, when run without parameter constraints, *rsp* values jump to 2.23 and 1.29 in 2013 and 2015, respectively (Table S3a), being about 10-fold higher than the constrained value. Other fine fitting parameters (e.g. *mx*, *m_s*) and other fine fitting functions also face the same problem (Table S3a). Without parameter constraints, unreasonable reconstructed growth curves and hence questionable phenological metrics can be retrieved (Table S3b).

Figure 6 presents the goodness-of-fit and extracted phenological metrics of fine fitting with AG at CA-NS6, performed with *phenofit*'s function *get_pheno* for every growing season during 2010–2016. The original and reconstructed EVI time series are presented in the left column, as well as the goodness-of-fit indices, including the correlation of determination (R^2), the Nash-Sutcliffe model efficiency coefficient (NSE), and the Root Mean Square Error (RMSE). The extracted phenological metrics are presented in columns two to five, which corresponds to the phenology extraction methods of TRS, DES, inflection and Gu, respectively. Meanwhile, phenological metrics are also retrieved in both *doy* and *date* units by function *get_pheno* (Table S4). They can be used directly without further conversion.

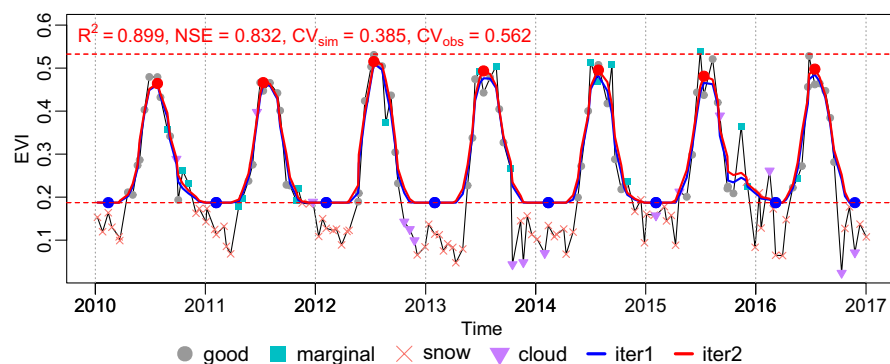


FIGURE 4 Rough fitting and growing season division at site 'CA-NS6' over Jan 2010 to Dec 2016 using MOD13A1 Collection 6 16-day EVI as input. The horizontal red dash lines are the lower and upper boundary (*ylu*) of time series y ; The black line is the original EVI time series; 'iter1' and 'iter2' are the 1st and 2nd iteration of rough fitting using *wWHIT*. Blue points and red points correspond to troughs and peaks detected in the growing season division module. The performance metrics of rough fitting are shown at the top of the plot, including coefficient of determination (R^2), Nash-Sutcliffe model efficiency coefficient (NSE), and observed coefficient of variation (CV_{obs}) and simulated coefficient of variation (CV_{sim}).

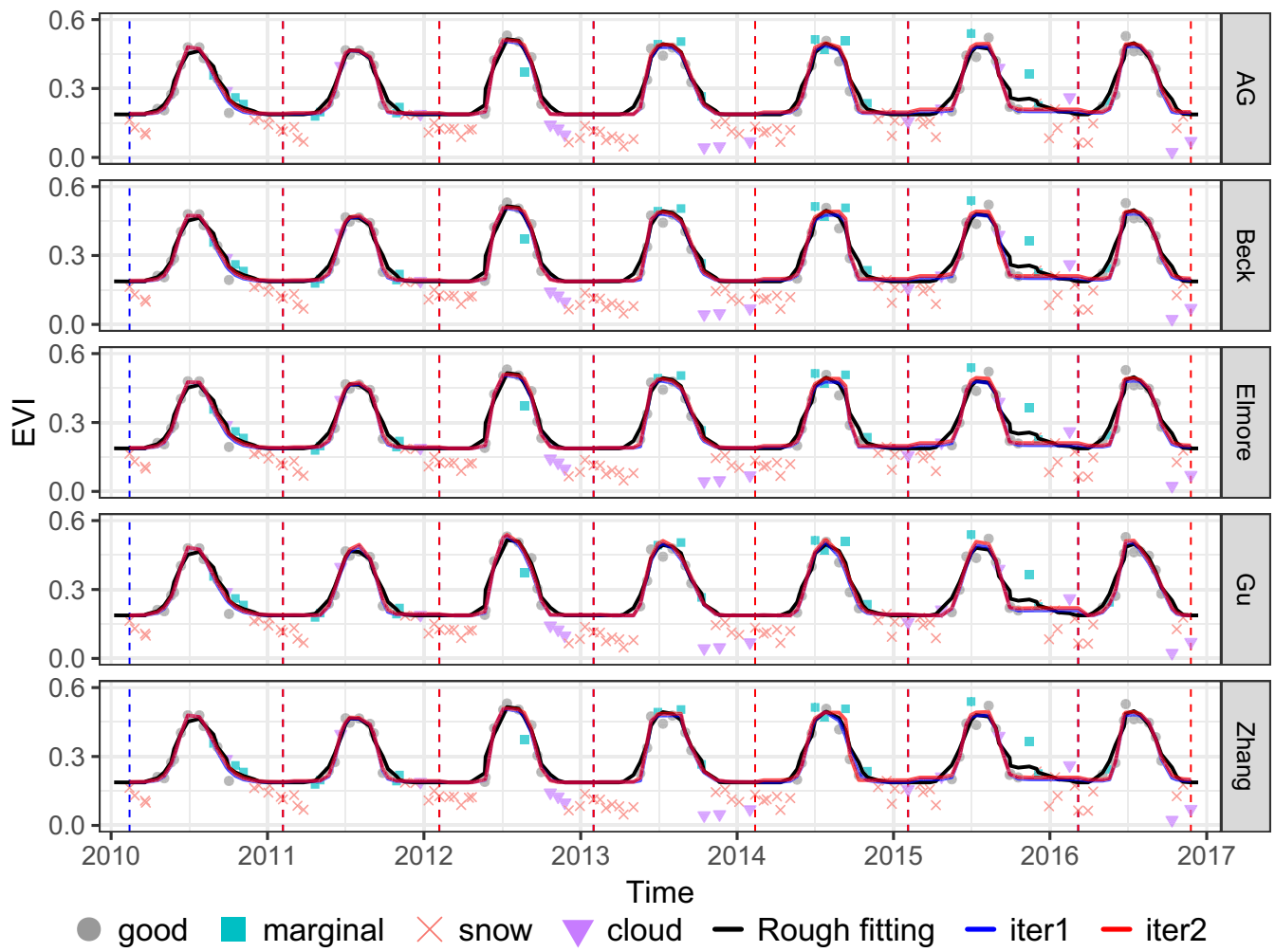


FIGURE 5 Results for the five fine curve fitting methods (identified at the right-hand side of the sub-plots) at site 'CA-NS6' over Jan 2010 to Dec 2016 using MOD13A1 Collection 6 16-day EVI as input. The black line is the final smoothed result of rough fitting wWHIT. 'iter1' and 'iter2' are the 1st and 2nd iteration of fine fitting. The vertical blue (red) dash lines are the start (end) of the growing season. Note that the end of the previous growing season often overlaps with the start time of the next growing season. Hence, only the vertical red dash lines are visible after 2011

4.2 | Application to regional scale

Phenology extraction can be easily extended from site scale to regional scale in *phenofit*. As phenology extraction is more challenging in regions with multiple growing seasons, we selected Henan province (Figure S3), one of the biggest farming provinces in China. In this region, 59.3% of the farming area has more than one growing seasons each calendar year (Guo et al., 2021).

Before applying *phenofit* spatially, users should determine the appropriate parameters to be used. The following steps are recommended: (a) sample representative points from the spatial data; (b) select the appropriate parameters by visually inspecting the performance of *phenofit* for those representative points and (c) finally map those selected parameters spatially according to the principle that same or similar land covers share the same parameters.

Figure S4 presents the number of growing seasons detected by *phenofit* in Henan province in 2015. The percentage of single, double and triple growing season regions are 39.4%, 53.8% and 6.8%,

respectively. The single-season region is located in the western and southern mountainous area of Henan, where the dominant land covers are forest and natural grassland in the western and single-season rice in the southern areas. The double-season region is located in the eastern plain, which is the main cropland area in Henan, where the first growing season corresponds to winter wheat and the second season to maize or soybean. The triple-season region is distributed sporadically in northern Henan, where vegetables are planted. Those ratios of single, double and triple growing season regions, as well as their spatial distribution, concur with results from Guo et al. (2021), being 40.7%, 57.8% and 1.5% in the same order and same region. Based on Sentinel-2 high-resolution imagery, Guo et al. (2021) used a more elaborate algorithm to divide growing seasons, which combines NDVI and a land surface water index to better distinguish growing season patterns. The similar results confirm that *phenofit* can divide growing season stably and reliably.

Figures 7, S5 and S6 exhibit extracted phenological metrics for Henan province at the first-, second- and third-growing seasons of

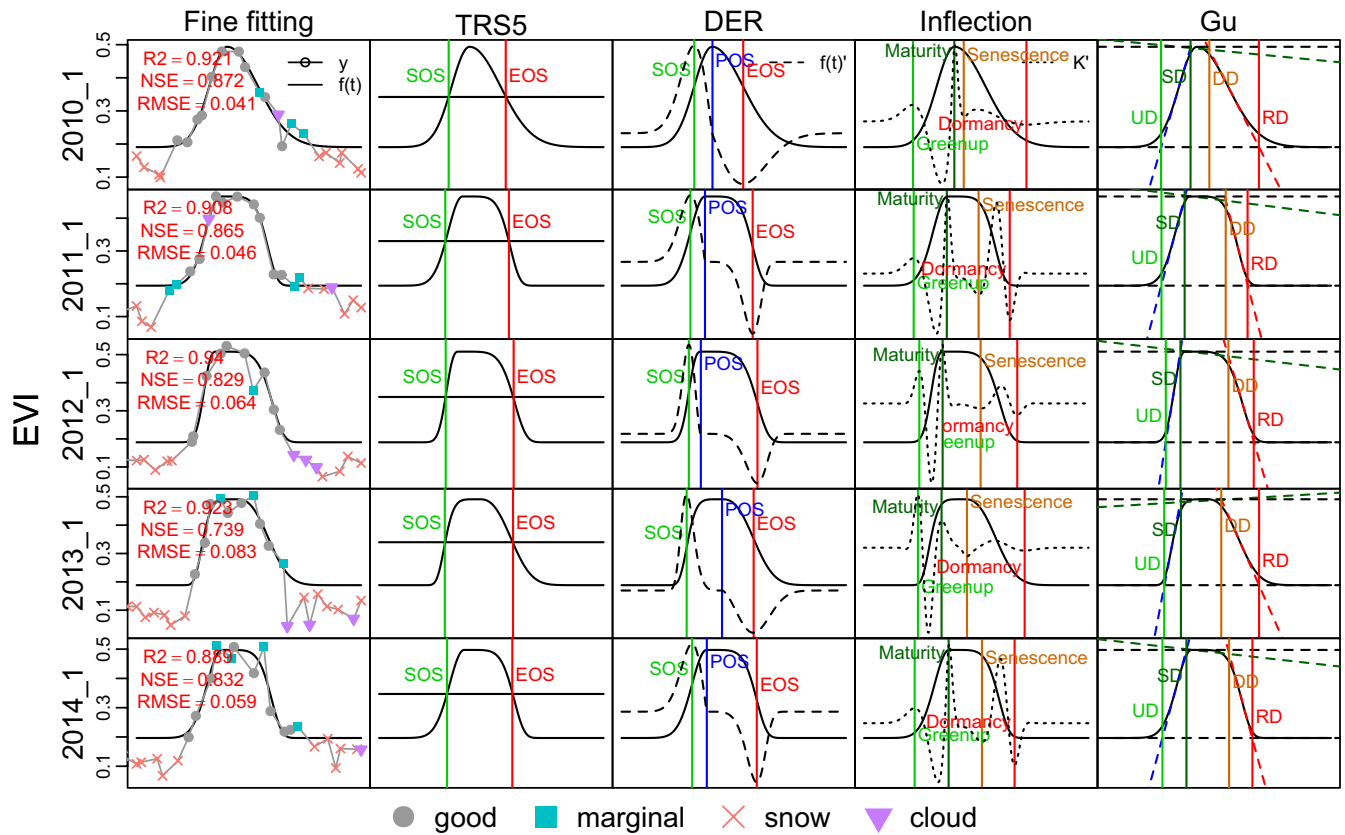
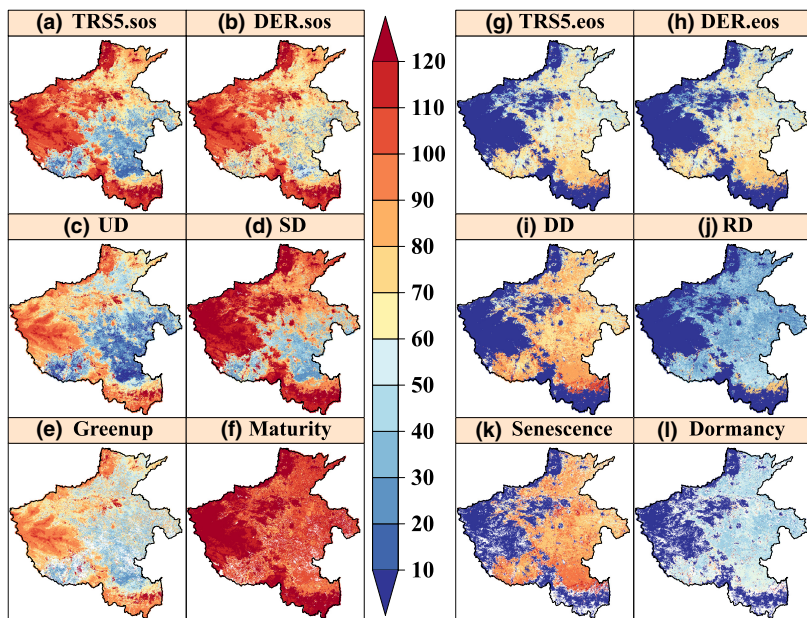


FIGURE 6 Phenology metrics of fine fitting AG at site 'CA-NS6'. The first column is the result of fine fitting. The remaining 4 columns are corresponding to the extracted phenological metrics of TRS, DER, Inflection, and Gu methods respectively. TRS5 is the abbreviation of TRS method with the threshold of 0.5. Detailed definitions of those phenological metrics can be found in Figure 3. $f(t)$ is the smoothed daily EVI time series by fine fitting (Fine fitting column, black lines); $f(t)'$ is the first-order derivative of $f(t)$ (DER column, long-dash lines); K' is the rate of change of curvature (Inflection column, dotted lines). Due to limited space, only the first 5 years are presented. This plot is produced by the function `get_pheno` by setting the parameter `IsPlot = TRUE`



2015. The distribution of those phenological metrics has a good consistency with land covers and the terrain, implying that the extracted phenological metrics are reasonable. Although phenological metrics

defined by different phenology extraction methods have different ecological meanings, phenological metrics defined by TRS, DER and Gu have similar spatial patterns, despite some differences in value.

FIGURE 7 Extracted phenological metrics for Henan province during the 1st growing season of 2015 using MOD13A2 Collection 6 16-day EVI as input, where rough fitting function `wWHIT` and fine fitting function Beck logistic was used. The left (a-f) and right (g-l) parts are phenological metrics during green-up and browning season respectively. In (e), (f), (k), and (l), white areas represent no retrieval, where the inflection method is failed to extract phenological metrics. TRS5 is the abbreviation of the TRS method with the threshold of 0.5; sos (eos) is the start (end) of the growing season. A detailed explanation of other phenological metrics can be found in Figure 3

Compared with other methods, the inflection method is less stable, especially in the greenup season (Figure 7; Figure S4). This is mainly because the inflection method has the most stringent requirement, where VI's change rate of curvature K_f should have two local maxima and two local minima values at the same time. Under frequent contamination or multiple growing season regions, the number of good-quality VI observations is limited, VI time series fluctuates unexpectedly and the requirement of inflection method can be broken frequently. Hence, in *phenofit*, the inflection method under these circumstances is not recommended.

4.3 | Comparison of *phenofit* with TIMESAT and *phenopix*

4.3.1 | On the situation of frequent contamination: Test data 1

Fine fitting was applied to reconstruct daily VI time series for Test Data 1 in every growing season, which reflects the performance of growing season division and directly determines the accuracy of the subsequent extracted phenological metrics. Figure 8 illustrates the performances of fine fitting with *phenofit*, TIMESAT and *phenopix*. Results show that they all successfully reconstructed VI time series in most cases, but the performances vary substantially in the non-growing season and the situation when VIs are contaminated. *phenopix*, which does not have a weight updating module, are more sensitive to outliers, for example, in the autumn of 2014 (Figure 8). When contaminated, *phenopix*'s parameters often become non-convergent, for example, in 2015 (Figure 8). For TIMESAT, the cut-off function and global model function make the reconstructed daily time series stable and smooth (Jönsson & Eklundh, 2004). Nevertheless, background values from TIMESAT and *phenopix* vary

substantially across years, for example, in 2013–2014 and 2015–2016 (Figure 8). As Shen et al. (2013) revealed, unreliable background VI values (i.e. VI values in the non-growing season) will introduce an apparent error of extracted phenological metrics, especially for the TRS method. In comparison, *phenofit* adopts the method of Zhang et al. (2007) and Zhang (2015), that is, includes previous and subsequent *nextend* good-quality observations in the fine fitting procedure to solve this problem. Additionally, the weight updating module in *phenofit* largely avoids the interference of contamination and achieves a robust performance.

4.3.2 | On the situation of multiple growing seasons and changing land cover: Test data 2

Figure 9 illustrates the performance of *phenofit* and TIMESAT in the situation of multiple growing seasons and changing land cover (i.e. based on Test Data 2, the synthesized VI time series introduced in Section 3.2). Because *phenopix* lacks a growing season division module, we did not use it in the following comparison. Figure 9 shows that *phenofit*'s rough fitting function *wWHIT* can effectively reduce the interference of noise and successfully capture the seasonal signals, and correctly delineate the double growing seasons and triple growing seasons patterns during 2012–2013 and 2014–2015, respectively. As long as *phenofit*'s rough fitting and growing season division modules work reliably, fine fitting (red line in Figure 9) and the final extracted phenological metrics are successfully obtained. In comparison, while TIMESAT successfully detected the single growing season in 2010–2011 and two growing seasons in 2013–2014, it failed to recognize the triple growing seasons in 2014–2015 (Table S5). Even though TIMESAT's rough fitting function works satisfactorily, TIMESAT is unable to recognize the changing growing seasons (blue line in Figure 9). When TIMESAT's growing season division

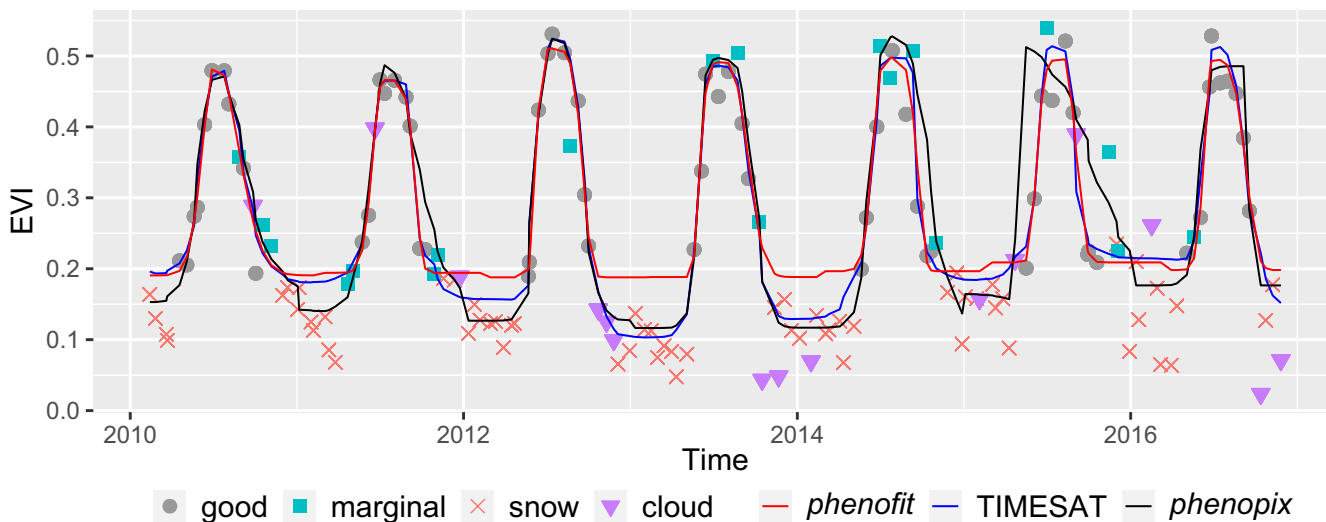


FIGURE 8 Comparison of *phenofit* with TIMESAT and *phenopix* at site 'CA-NS6' during 2010–2016, using MOD13A1 Collection 6 16-day EVI as input. For *phenofit* and TIMESAT, in the procedure of fine fitting, the Asymmetric Gaussian (AG) was used, whereas for *phenopix* the Beck logistic was employed because AG is not part of *phenopix*

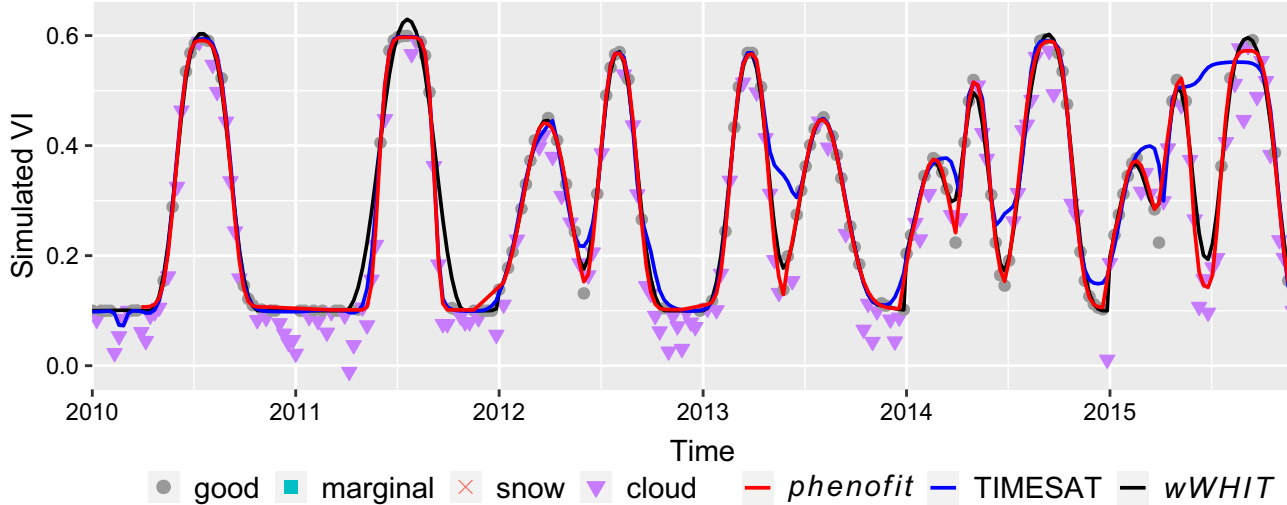


FIGURE 9 Comparison of *phenofit* with TIMESAT based on simulated vegetation index during 2010–2015. For *phenofit* and TIMESAT, in the procedure of fine fitting, the Asymmetric Gaussian (AG) was used. One growing season was simulated for the first 2 years (i.e. 2010 and 2011), two growing seasons for the next 2 years (i.e. 2012 and 2013), and three growing seasons for the final 2 years (i.e. 2014 and 2015)

is incorrect, its fine fitting module will lose the ability to simulate the vegetation growth curve (e.g. the second half-year of 2015 in Figure 9), which finally results in an apparent error in TIMESAT's extracted phenological metrics (with the bias rising to 151 days, Table S5).

Whether the retrieved phenological metrics effectively represent real transition dates highly relies on the performance of rough fitting and growing season division. Users should select rough fitting functions and their parameters carefully. We suggest using *wHANTS* for natural vegetation, such as forests and shrublands, which experience limited multi-annual variation; and using *wWHIT* for agricultural areas where crop rotation can result in very different temporal patterns from 1 year to the next. Detailed suggestions on parameters' selection are provided in Section 2.3.

4.4 | The uncertainty of *phenofit*'s outputs

The uncertainty of *phenofit*'s outputs is mainly derived from the growing season division module, especially for regions with multiple growing seasons per year. Figure 10 further illustrates the performance and uncertainty of *phenofit*'s growing season division based on Test Data 3 (i.e. the 9 FLUXNET2015 flux sites with multiple growing seasons introduced in Section 3.3). In most situations, *phenofit* can divide growing seasons correctly, including growing seasons with low amplitude (e.g. Figure 10a,c,f,g). *phenofit* used many empirical and practical strategies to eliminate unrealistic troughs and peaks, which contributes to the stable performance in growing season division, even for cropland and grassland (Figure 10c,g,h).

Users should be aware that *phenofit* cannot perfectly solve the problem of growing season division in every instance. First, if rough fitting results have very limited temporal variability in VI values, it will lose the regional extreme values, hence peaks and

troughs (e.g. in 2012 of Figure 10b). To avoid undue influence of cloud, cloud shadow, snow and other types of contamination in the curve fitting procedure, *phenofit* adjusts data-point weights and curve-fitting results to approach the upper envelope, which will inevitably weaken or even confound real vegetation seasonal signals. This leads to errors in growing season division and phenology extraction. Second, under drought or heatwave, VI values will drop sharply, for example, the prevalent European heatwave and drought in 2003, as seen in Figure 10d,e (Zhang et al., 2016). In that situation, the shape of the VI time series looks like two growing seasons (e.g. in 2003 of Figure 10e), but actually only one exists. *phenofit* has limited ability to distinguish the real growing season under severe heatwaves or droughts. How to best resolve this issue is still an open question in ecological studies and further research is required.

4.5 | The potential application of *phenofit* for high-resolution imagery

Besides MODIS, *phenofit* can be also extended to extract vegetation phenology from other high-resolution satellites, for example, Sentinel-2 (Drusch et al., 2012; Jönsson et al., 2018; Tian et al., 2021) and Landsat (Loveland & Dwyer, 2012; Melaas et al., 2013, 2016). As long as the satellite-derived VIs have enough observations to distinguish key points of the vegetation growth curve, *phenofit* will be suitable for phenology extraction. *phenofit* can be also used for radar imagery, such as Sentinel-1. Previous studies found that VIs derived from radar satellites, for example the Radar Vegetation Index (Kim et al., 2012) and Cross Ratio (Meroni et al., 2021; Vreugdenhil et al., 2018, 2020), have high linear correlations with Normalized Difference Vegetation Index, Vegetation Optical Depth over croplands and grasslands. Radar imagery is not hampered by cloud cover, so VIs derived from radar satellites are complementary

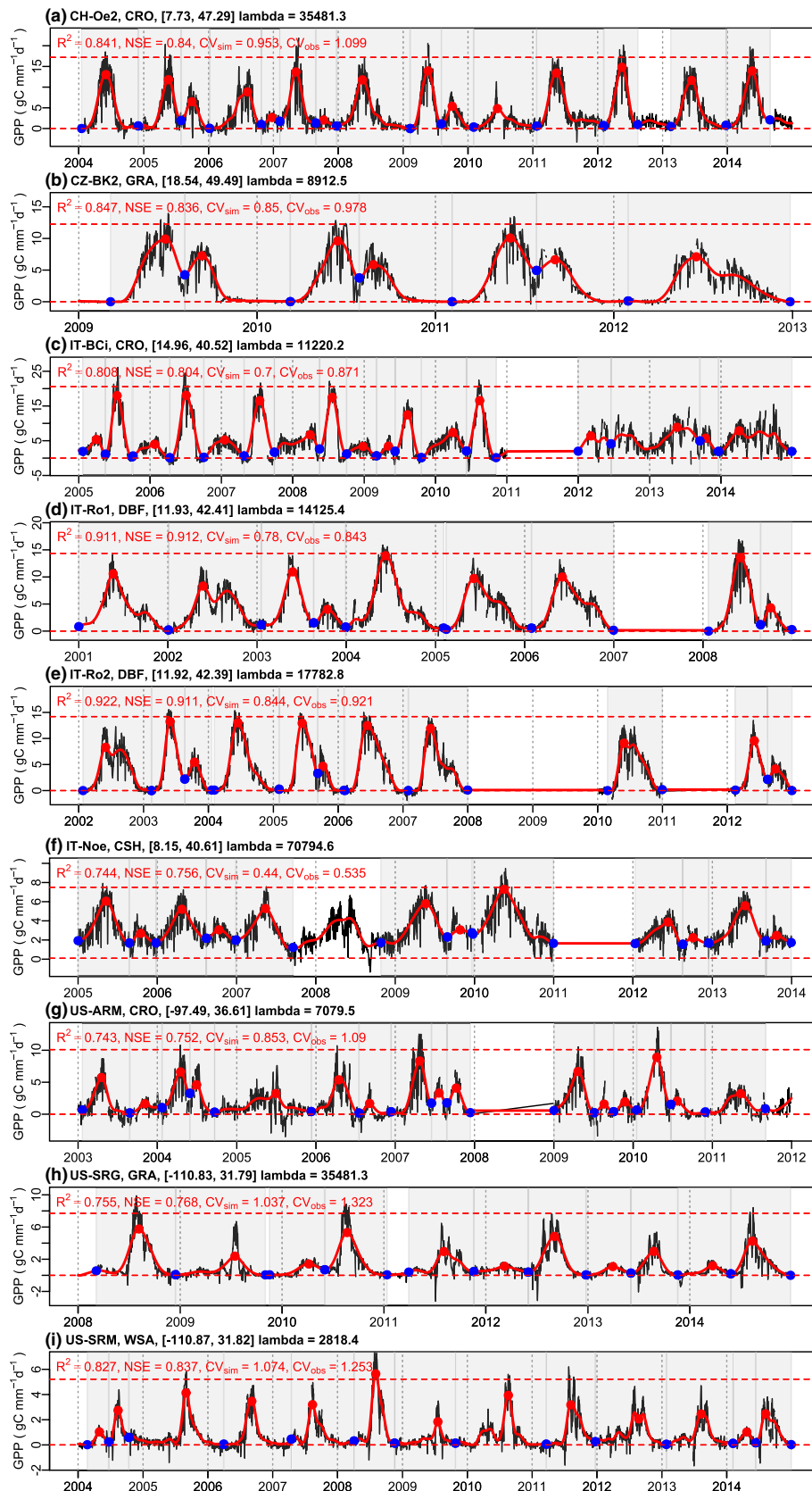


FIGURE 10 Performance of *phenofit*'s growing cycle division on the representative multiple growing season flux sites. Flux site's name, vegetation IGBP type, site coordinates ([latitude, longitude]), wWHIT's parameter lambda (automatically determined by V-curve theory) are presented in the subplot title. To preserve the growing seasons with a low amplitude, wWHIT rough fitting (red line) was applied only once. Blue points and red points correspond to the troughs and peaks estimated during the growing season division implementation. Two troughs define a growing season, colored by grey

to those derived from optical satellites (Andela et al., 2013; Meroni et al., 2021). Because high-resolution satellites have a relatively coarse temporal frequency, the vegetation growth curve from their composited VIs may fluctuate sharply and may not follow the logistic curve. Hence, fine fitting is unnecessary in such a situation, and the result of rough fitting is suggested to extract vegetation phenology. Due to the same reason and the stringent requirement (see Section 4.2), the inflection method is not suggested for high-resolution satellites' phenology extraction in *phenofit*.

Figures S7 and S8 present an example of using Sentinel-2 EVI time series to extract vegetation phenology at a small village in Henan Province (Figure S3d), which has $123 \times 118 = 14,514$ Sentinel-2 10 m \times 10 m pixels in the spatial domain. The dominant land cover is double-growing season cropland, with the first season of winter wheat (typically from October and harvested in late May–early June the next year) and the second season of maize (typically mid-June to late September–early October, McVicar et al., 2002). Generally, phenological metrics extracted from rough fitting match well with these land cover types. This implies the success of *phenofit* in the application of Sentinel-2. However, *phenofit* has the following shortcomings when applied to high-resolution satellite VI data: (a) *phenofit* only uses the VI observations of the current growing season to extract vegetation phenology. Under this strategy, in the situation of very limited observations in the current growing season, *phenofit* will lose its ability to reconstruct VI and extract phenology. With a relatively low revisit frequency plus potential contamination (Li & Roy, 2017), high-resolution imagery is more likely to run into the above-mentioned issue. The strategy, that combines observations of different years in phenology estimation (Bolton et al., 2020; Jönsson et al., 2018; Li et al., 2017; Melaas et al., 2013, 2016; Tian et al., 2021), needs to be implemented in *phenofit*'s future maintenance; and (b) *phenofit* is written in R, and its computational efficiency requires improvement for large-scale analysis with high-resolution satellite images as input.

5 | CONCLUSIONS

We present and evaluate an open-source vegetation phenology extraction package in R language, called *phenofit*. *phenofit* is designed to reconstruct vegetation daily time series and extract vegetation phenology from satellite-derived VIs, even if they are frequently contaminated. Besides application to coarse-resolution data of high frequency, as for example from MODIS and AVHRR, *phenofit* also works for VIs from other kinds of sources, such as VIs from high-resolution optical satellites (e.g. Sentinel-2 and Landsat) and radar satellites (e.g. Sentinel-1), vegetation greenness indices from digital cameras and gross primary production from eddy-covariance sites. From a functional perspective, *phenofit* adopts state-of-the-art methods for (a) rough fitting, (b) weight updating, (c) growing season division, (d) fine fitting and (e) phenology extraction functions, which makes phenology extraction more accurate and easier to implement. From a software development perspective, *phenofit* is open source and offers a suite of standardized and reproducible scripts that can

be further improved and developed by other researchers. Compared against TIMESAT, *phenofit* provides flexible input and output options, a practical growing season division function, rich curve fitting and phenology extraction functions. Compared against *phenopix*, *phenofit* has a robust performance under different kinds of optical noise.

Major future developments of *phenofit* currently earmarked include the following: (a) promoting computational efficiency that will make *phenofit* comparable to the Fortran implementation of TIMESAT using the *Julia* languages (<https://github.com/eco-hydro/phenofit.jl>); For example, taking MOD13A2 16-day EVI as input, phenology extraction on 1,000,000 pixels and 6 years currently costs about 35 hr with 10 CPU cores in parallel (Table S6). When the kernel scripts are rewritten in *Julia*, it is expected to be 5–10 times faster. (b) Improving the performance in regions with multiple growing seasons in a year; (c) incorporating robust fitting approaches for time series with lower temporal frequency, such as from Sentinel-2 satellites; and (d) adding modules to quantify the uncertainty of the extracted phenological metrics. *phenofit* can contribute to the study of ecological process dynamics and assist in effective modelling of global change impacts on vegetation, as caused by climate variability and human intervention.

ACKNOWLEDGEMENTS

This study was supported by the National Natural Science Foundation of China (Grant 4210011820), the Fundamental Research Funds for the Central Universities and China University of Geosciences (Wuhan) (Grant CUG2106107). We acknowledge the FLUXNET community for the flux sites' eddy-covariance GPP data. We thank the Senior Editor, Professor Robert Freckleton and two anonymous reviewers for their critical and timely assessment of the manuscript. We appreciate the patient guidance of Paul H. C. Eilers about the Whittaker smoother. We also acknowledge Jianjian Cui, who helped visually inspect the performance of growing season division.

CONFLICT OF INTEREST

The authors declare no conflict of interest.

AUTHORS' CONTRIBUTIONS

Dongdong Kong designed the *phenofit*; Dongdong Kong and Mingzhong Xiao wrote *phenofit* in R and completed the first draft; Xihui Gu is the research project administrator; all authors contributed to the writing and reviewing of the article.

PEER REVIEW

The peer review history for this article is available at <https://publon.com/publon/10.1111/2041-210X.13870>.

DATA AVAILABILITY STATEMENT

The *phenofit* package in the version of v0.3.5 is available at <https://github.com/eco-hydro/phenofit> and <https://zenodo.org/recor/d/6320537> (Kong, 2022b), which can be easily installed using the

R script: ‘`remotes::install_github("eco-hydro/phenofit")`’. Code and data of case studies are available at <https://zenodo.org/recor d/6425745> (Kong, 2022a). The documentation of R package `phenofit` is at <http://phenofit.top>. TIMESAT used in this study is at <https://zenodo.org/record/5150216> (Kong, 2021). The eddy-covariance GPP estimations from flux sites can be found at <https://fluxnet.org/data/fluxnet2015-dataset/>.

ORCID

Dongdong Kong  <https://orcid.org/0000-0003-1836-8172>

Tim R. McVicar  <https://orcid.org/0000-0002-0877-8285>

Mingzhong Xiao  <https://orcid.org/0000-0002-9462-2577>

Yongqiang Zhang  <https://orcid.org/0000-0002-3562-2323>

Jorge L. Peña-Arancibia  <https://orcid.org/0000-0002-4952-9293>

Gianluca Filippa  <https://orcid.org/0000-0002-4554-6045>

Xihui Gu  <https://orcid.org/0000-0002-1924-9282>

REFERENCES

- Alleaume, S., Dusseux, P., Thierion, V., Commagnac, L., Laventure, S., Lang, M., Féret, J. B., Hubert-Moy, L., & Luque, S. (2018). A generic remote sensing approach to derive operational essential biodiversity variables (EBVs) for conservation planning. *Methods in Ecology and Evolution*, 9(8), 1822–1836. <https://doi.org/10.1111/2041-210X.13033>
- Andela, N., Liu, Y. Y., van Dijk, A. I. J. M., de Jeu, R. A. M., & McVicar, T. R. (2013). Global changes in dryland vegetation dynamics (1988–2008) assessed by satellite remote sensing: Comparing a new passive microwave vegetation density record with reflective greenness data. *Biogeosciences*, 10(10), 6657–6676. <https://doi.org/10.5194/bg-10-6657-2013>
- Atzberger, C., & Eilers, P. H. C. (2011). Evaluating the effectiveness of smoothing algorithms in the absence of ground reference measurements. *International Journal of Remote Sensing*, 32(13), 3689–3709. <https://doi.org/10.1080/01431161003762405>
- Barichivich, J., Briffa, K. R., Myneni, R. B., Osborn, T. J., Melvin, T. M., Ciais, P., Piao, S., & Tucker, C. (2013). Large-scale variations in the vegetation growing season and annual cycle of atmospheric CO₂ at high northern latitudes from 1950 to 2011. *Global Change Biology*, 19(10), 3167–3183. <https://doi.org/10.1111/gcb.12283>
- Beck, P. S. A., Atzberger, C., Høgda, K. A., Johansen, B., & Skidmore, A. K. (2006). Improved monitoring of vegetation dynamics at very high latitudes: A new method using MODIS NDVI. *Remote Sensing of Environment*, 100(3), 321–334. <https://doi.org/10.1016/j.rse.2005.10.021>
- Bolton, D. K., Gray, J. M., Melaas, E. K., Moon, M., Eklundh, L., & Friedl, M. A. (2020). Continental-scale land surface phenology from harmonized Landsat 8 and Sentinel-2 imagery. *Remote Sensing of Environment*, 240(April), 111685. <https://doi.org/10.1016/j.rse.2020.111685>
- Bush, E. R., Abernethy, K. A., Jeffery, K., Tutin, C., White, L., Dimoto, E., Dikangadissi, J. T., Jump, A. S., & Bunnefeld, N. (2017). Fourier analysis to detect phenological cycles using long-term tropical field data and simulations. *Methods in Ecology and Evolution*, 8(5), 530–540. <https://doi.org/10.1111/2041-210X.12704>
- Cao, R., Chen, Y., Shen, M., Chen, J., Zhou, J., Wang, C., & Yang, W. (2018). A simple method to improve the quality of NDVI time-series data by integrating spatiotemporal information with the Savitzky-Golay filter. *Remote Sensing of Environment*, 217(November), 244–257. <https://doi.org/10.1016/j.rse.2018.08.022>
- Chen, J., Jönsson, P., Tamura, M., Gu, Z., Matsushita, B., & Eklundh, L. (2004). A simple method for reconstructing a high-quality NDVI time-series data set based on the Savitzky–Golay filter. *Remote Sensing of Environment*, 91(3–4), 332–344. <https://doi.org/10.1016/j.rse.2004.03.014>
- Chuine, I., & Beaubien, E. G. (2001). Phenology is a major determinant of tree species range. *Ecology Letters*, 4(5), 500–510. <https://doi.org/10.1046/j.1461-0248.2001.00261.x>
- Cihlar, J., Ly, H., Li, Z., Chen, J., Pokrant, H., & Huang, F. (1997). Multitemporal, multichannel AVHRR data sets for land biosphere studies – Artifacts and corrections. *Remote Sensing of Environment*, 60(1), 35–57. [https://doi.org/10.1016/S0034-4257\(96\)00137-X](https://doi.org/10.1016/S0034-4257(96)00137-X)
- Cleveland, W. S. (1979). Robust locally weighted regression and smoothing scatterplots. *Journal of the American Statistical Association*, 74(368), 829–836. <https://doi.org/10.1080/01621459.1979.10481038>
- Coluzzi, R., Imbrenda, V., Lanfredi, M., & Simonello, T. (2018). A first assessment of the Sentinel-2 level 1-C cloud mask product to support informed surface analyses. *Remote Sensing of Environment*, 217(October 2017), 426–443. <https://doi.org/10.1016/j.rse.2018.08.009>
- Didan, K., Munoz, A. B., & Huete, A. (2015). MODIS Vegetation Index User's Guide (MOD13 Series), 2015(June).
- Dong, J., Metternicht, G., Hostert, P., Fensholt, R., & Chowdhury, R. R. (2019). Remote sensing and geospatial technologies in support of a normative land system science: Status and prospects. *Current Opinion in Environmental Sustainability*, 38, 44–52. <https://doi.org/10.1016/j.cosust.2019.05.003>
- Drusch, M., Del Bello, U., Carlier, S., Colin, O., Fernandez, V., Gascon, F., Hoersch, B., Isola, C., Laberinti, P., Martimort, P., Meygret, A., Spoto, F., Sy, O., Marchese, F., & Bargellini, P. (2012). Sentinel-2: ESA's optical high-resolution mission for GMES operational services. *Remote Sensing of Environment*, 120, 25–36. <https://doi.org/10.1016/j.rse.2011.11.026>
- Eilers, P. H. C. (2003). A perfect smoother. *Analytical Chemistry*, 75(14), 3631–3636. <https://doi.org/10.1021/ac034173t>
- Eilers, P. H. C., Pesendorfer, V., & Bonifacio, R. (2017). Automatic smoothing of remote sensing data. 2017 9th International Workshop on the Analysis of Multitemporal Remote Sensing Images, MultiTemp 2017, (D). <https://doi.org/10.1109/Multi-Temp.2017.8076705>
- Eklundh, L., & Jönsson, P. (2017). TIMESAT 3.3 with seasonal trend decomposition and parallel processing software manual. Retrieved from https://web.nateko.lu.se/timesat/docs/TIMESAT33_SoftwareManual.pdf
- Elmore, A. J., Guinn, S. M., Minsley, B. J., & Richardson, A. D. (2012). Landscape controls on the timing of spring, autumn, and growing season length in mid-Atlantic forests. *Global Change Biology*, 18(2), 656–674. <https://doi.org/10.1111/j.1365-2486.2011.02521.x>
- Fensholt, R., Horion, S., Tagesson, T., Ehammar, A., Ivits, E., & Rasmussen, K. (2015). Global-scale mapping of changes in ecosystem functioning from earth observation-based trends in total and recurrent vegetation. *Global Ecology and Biogeography*, 24(9), 1003–1017. <https://doi.org/10.1111/geb.12338>
- Filippa, G., Cremonese, E., Migliavacca, M., Galvagno, M., Forkel, M., Wingate, L., Tomelleri, E., Morra di Cellia, U., & Richardson, A. D. (2016). Phenopix: A R package for image-based vegetation phenology. *Agricultural and Forest Meteorology*, 220, 141–150. <https://doi.org/10.1016/j.agrformet.2016.01.006>
- Forkel, M., Migliavacca, M., Thonicke, K., Reichstein, M., Schaphoff, S., Weber, U., & Carvalhais, N. (2015). Codominant water control on global interannual variability and trends in land surface phenology and greenness. *Global Change Biology*, 21, 3414–3435. <https://doi.org/10.1111/gcb.12950>
- Frasso, G., & Eilers, P. H. C. (2015). L- and V-curves for optimal smoothing. *Statistical Modelling*, 15(1), 91–111. <https://doi.org/10.1177/1471082X14549288>
- Goulden, M. (2016). FLUXNET2015 CA-NS6 UCI-1989 burn site. <https://doi.org/10.18140/FLX/1440041>

- Gu, L., Post, W. M., Baldocchi, D. D., Black, T. A., Suyker, A. E., Verma, S. B., Vesala, T., & Wofsy, S. C. (2009). Characterizing the seasonal dynamics of plant community photosynthesis across a range of vegetation types. In A. Noormets (Ed.), *Phenology of ecosystem processes: Applications in global change research* (pp. 35–58). Springer New York. https://doi.org/10.1007/978-1-4419-0026-5_2
- Guo, Y., Xia, H., Pan, L., Zhao, X., Li, R., Bian, X., Wang, R., & Yu, C. (2021). Development of a new phenology algorithm for fine mapping of cropping intensity in complex planting areas using sentinel-2 and google earth engine. *ISPRS International Journal of Geo-Information*, 10(9), 587. <https://doi.org/10.3390/ijgi10090587>
- Harwood, T. D., Donohue, R. J., Williams, K. J., Ferrier, S., McVicar, T. R., Newell, G., & White, M. (2016). Habitat Condition Assessment System: A new way to assess the condition of natural habitats for terrestrial biodiversity across whole regions using remote sensing data. *Methods in Ecology and Evolution*, 7(9), 1050–1059. <https://doi.org/10.1111/2041-210X.12579>
- Hilker, T., Lyapustin, A. I., Tucker, C. J., Sellers, P. J., Hall, F. G., & Wang, Y. (2012). Remote sensing of tropical ecosystems: Atmospheric correction and cloud masking matter. *Remote Sensing of Environment*, 127, 370–384. <https://doi.org/10.1016/j.rse.2012.08.035>
- Holben, B. N. (1986). Characteristics of maximum-value composite images from temporal AVHRR data. *International Journal of Remote Sensing*, 7(11), 1417–1434. <https://doi.org/10.1080/01431168608948945>
- Huete, A., Didan, K., Miura, T., Rodriguez, E., Gao, X., & Ferreira, L. (2002). Overview of the radiometric and biophysical performance of the MODIS vegetation indices. *Remote Sensing of Environment*, 83(1–2), 195–213. [https://doi.org/10.1016/S0034-4257\(02\)00096-2](https://doi.org/10.1016/S0034-4257(02)00096-2)
- Hufkens, K., Basler, D., Milliman, T., Melaas, E. K., & Richardson, A. D. (2018). An integrated phenology modelling framework in R. *Methods in Ecology and Evolution*, 9(5), 1276–1285. <https://doi.org/10.1111/2041-210X.12970>
- Joiner, J., Yoshida, Y., Zhang, Y., Duveiller, G., Jung, M., Lyapustin, A., Wang, Y., & Tucker, C. (2018). Estimation of terrestrial global gross primary production (GPP) with satellite data-driven models and eddy covariance flux data. *Remote Sensing*, 10(9), 1–38. <https://doi.org/10.3390/rs10091346>
- Jönsson, P., Cai, Z., Melaas, E., Friedl, M. A., & Eklundh, L. (2018). A method for robust estimation of vegetation seasonality from Landsat and Sentinel-2 time series data. *Remote Sensing*, 10(4), 635. <https://doi.org/10.3390/rs10040635>
- Jönsson, P., & Eklundh, L. (2002). Seasonality extraction by function fitting to time-series of satellite sensor data. *IEEE Transactions on Geoscience and Remote Sensing*, 40(8), 1824–1832. <https://doi.org/10.1109/TGRS.2002.802519>
- Jönsson, P., & Eklundh, L. (2004). TIMESAT – A program for analyzing time-series of satellite sensor data. *Computers and Geosciences*, 30(8), 833–845. <https://doi.org/10.1016/j.cageo.2004.05.006>
- Kim, Y., Jackson, T., Bindlish, R., Lee, H., & Hong, S. (2012). Radar vegetation index for estimating the vegetation water content of rice and soybean. *IEEE Geoscience and Remote Sensing Letters*, 9(4), 564–568. <https://doi.org/10.1109/LGRS.2011.2174772>
- Klosterman, S. T., Hufkens, K., Gray, J. M., Melaas, E., Sonnentag, O., Lavine, I., Mitchell, L., Norman, R., Friedl, M. A., & Richardson, A. D. (2014). Evaluating remote sensing of deciduous forest phenology at multiple spatial scales using PhenoCam imagery. *Biogeosciences*, 11(16), 4305–4320. <https://doi.org/10.5194/bg-11-4305-2014>
- Kong, D. (2021). R package: Extract remote sensing vegetation phenology by TIMESAT V3.3 Fortran library. Zenodo, <https://doi.org/10.5281/zenodo.5150216>
- Kong, D. (2022a). eco-hydro/phenofit-scripts: Phenofit examples in version 3.0 (v0.1.0). Zenodo, <https://doi.org/10.5281/zenodo.6425745>
- Kong, D. (2022b). R package: A state-of-the-art Vegetation Phenology extraction package, phenofit v0.3.5. Zenodo, <https://doi.org/10.5281/zenodo.6320537>
- Kong, D., Zhang, Y., Gu, X., & Wang, D. (2019). A robust method for reconstructing global MODIS EVI time series on the Google Earth Engine. *ISPRS Journal of Photogrammetry and Remote Sensing*, 155(May), 13–24. <https://doi.org/10.1016/j.isprsjprs.2019.06.014>
- Kong, D., Zhang, Y., Wang, D., Chen, J., & Gu, X. (2020). Photoperiod explains the asynchronization between vegetation carbon phenology and vegetation greenness phenology. *Journal of Geophysical Research: Biogeosciences*, 125(8), e2020JG005636. <https://doi.org/10.1029/2020JG005636>
- Lambin, E. F. (1999). Monitoring forest degradation in tropical regions by remote sensing: Some methodological issues. *Global Ecology and Biogeography*, 8(3–4), 191–198. <https://doi.org/10.1046/j.1365-2699.1999.00123.x>
- Lausch, A., Bastian, O., Klotz, S., Leitão, P. J., Jung, A., Rocchini, D., Schaeppman, M. E., Skidmore, A. K., Tischendorf, L., & Knapp, S. (2018). Understanding and assessing vegetation health by in situ species and remote-sensing approaches. *Methods in Ecology and Evolution*, 9(8), 1799–1809. <https://doi.org/10.1111/2041-210X.13025>
- Li, J., & Roy, D. P. (2017). A global analysis of sentinel-2a, sentinel-2b and Landsat-8 data revisit intervals and implications for terrestrial monitoring. *Remote Sensing*, 9(9), 902. <https://doi.org/10.3390/rs9090902>
- Li, X., Zhou, Y., Asrar, G. R., & Meng, L. (2017). Characterizing spatio-temporal dynamics in phenology of urban ecosystems based on Landsat data. *Science of The Total Environment*, 605–606, 721–734. <https://doi.org/10.1016/j.scitotenv.2017.06.245>
- Lian, X., Piao, S., Li, L. Z. X., Li, Y., Huntingford, C., Ciais, P., Cescatti, A., Janssens, I. A., Peñuelas, J., Buermann, W., Chen, A., Li, X., Myneni, R. B., Wang, X., Wang, Y., Yang, Y., Zeng, Z., Zhang, Y., & McVicar, T. R. (2020). Summer soil drying exacerbated by earlier spring greening of northern vegetation. *Science Advances*, 6(1), 1–12. <https://doi.org/10.1126/sciadv.aax0255>
- Lieth, H. (1974). *Phenology and seasonality modeling*. H. Lieth (Ed.) (Vol. 8). Springer Berlin Heidelberg. <https://doi.org/10.1007/978-3-642-51863-8>
- Loveland, T. R., & Dwyer, J. L. (2012). Landsat: Building a strong future. *Remote Sensing of Environment*, 122, 22–29. <https://doi.org/10.1016/j.rse.2011.09.022>
- Luo, Y., Zhang, Z., Chen, Y., Li, Z., & Tao, F. (2020). ChinaCropPhen1km: A high-resolution crop phenological dataset for three staple crops in China during 2000–2015 based on leaf area index (LAI) products. *Earth System Science Data*, 12(1), 197–214. <https://doi.org/10.5194/essd-12-197-2020>
- McVicar, T. R., & Jupp, D. L. B. (1998). The current and potential operational uses of remote sensing to aid decisions on drought exceptional circumstances in Australia: A review. *Agricultural Systems*, 57(3), 399–468. [https://doi.org/10.1016/S0308-521X\(98\)00026-2](https://doi.org/10.1016/S0308-521X(98)00026-2)
- McVicar, T. R., Zhang, G., Bradford, A. S., Wang, H., Dawes, W. R., Zhang, L., & Lingtao, L. (2002). Monitoring regional agricultural water use efficiency for Hebei Province on the North China Plain. *Australian Journal of Agricultural Research*, 53(1), 55. <https://doi.org/10.1071/AR00170>
- Melaas, E. K., Friedl, M. A., & Zhu, Z. (2013). Detecting interannual variation in deciduous broadleaf forest phenology using Landsat TM/ETM+ data. *Remote Sensing of Environment*, 132, 176–185. <https://doi.org/10.1016/j.rse.2013.01.011>
- Melaas, E. K., Sulla-Menashe, D., Gray, J. M., Black, T. A., Morin, T. H., Richardson, A. D., & Friedl, M. A. (2016). Multisite analysis of land surface phenology in North American temperate and boreal deciduous forests from Landsat. *Remote Sensing of Environment*, 186, 452–464. <https://doi.org/10.1016/j.rse.2016.09.014>
- Meroni, M., d'Andrimont, R., Vrieling, A., Fasbender, D., Lemoine, G., Rembold, F., Seguini, L., & Verhegghen, A. (2021). Comparing land surface phenology of major European crops as derived from SAR and multispectral data of Sentinel-1 and -2. *Remote Sensing*

- of Environment, 253(February), 112232. <https://doi.org/10.1016/j.rse.2020.112232>
- Moussus, J.-P., Julliard, R., & Jiguet, F. (2010). Featuring 10 phenological estimators using simulated data. *Methods in Ecology and Evolution*, 1(2), 140–150. <https://doi.org/10.1111/j.2041-210X.2010.00020.x>
- Palmer, S. C. J., Odermatt, D., Hunter, P. D., Brockmann, C., Présing, M., Balzter, H., & Tóth, V. R. (2015). Satellite remote sensing of phytoplankton phenology in Lake Balaton using 10 years of MERIS observations. *Remote Sensing of Environment*, 158, 441–452. <https://doi.org/10.1016/j.rse.2014.11.021>
- Pastorello, G., Trotta, C., Canfora, E., Chu, H., Christianson, D., Cheah, Y. W., Poindexter, C., Chen, J., Elbashandy, A., Humphrey, M., Isaac, P., Polidori, D., Reichstein, M., Ribeca, A., van Ingen, C., Vuichard, N., Zhang, L., Amiro, B., Ammann, C., ... Papale, D. (2020). The FLUXNET2015 dataset and the ONEFlux processing pipeline for eddy covariance data. *Scientific Data*, 7(1), 225. <https://doi.org/10.1038/s41597-020-0534-3>
- Peña-Arancibia, J. L., Mahboob, M. G., Islam, A. T., Mainuddin, M., Yu, Y., Ahmad, M. D., Ibn Murad, K. F., Saha, K. K., Hossain, A., Moniruzzaman, M., Ticehurst, C., & Kong, D. (2021). The green revolution from space: Mapping the historic dynamics of main rice types in one of the world's food bowls. *Remote Sensing Applications: Society and Environment*, 21(January), 100460. <https://doi.org/10.1016/j.rsase.2020.100460>
- Peñuelas, J., & Filella, I. (2001). Phenology: Responses to a warming world. *Science*, 294(5543), 793–795. <https://doi.org/10.1126/science.1066860>
- Peñuelas, J., Rutishauser, T., & Filella, I. (2009). Phenology feedbacks on climate change. *Science*, 324(5929), 887–888. <https://doi.org/10.1126/science.1173004>
- Piao, S., Friedlingstein, P., Ciais, P., Viovy, N., & Demarty, J. (2007). Growing season extension and its impact on terrestrial carbon cycle in the Northern Hemisphere over the past 2 decades. *Global Biogeochemical Cycles*, 21(3), GB3018. <https://doi.org/10.1029/2006GB002888>
- Piao, S., Liu, Q., Chen, A., Janssens, I. A., Fu, Y., Dai, J., Liu, L., Lian, X., Shen, M., & Zhu, X. (2019). Plant phenology and global climate change: Current progresses and challenges. *Global Change Biology*, 25, 1922–1940. <https://doi.org/10.1111/gcb.14619>
- Richardson, A. D., Hufkens, K., Milliman, T., Aubrecht, D. M., Chen, M., Gray, J. M., Johnston, M. R., Keenan, T. F., Klosterman, S. T., Kosmala, M., Melaas, E. K., Friedl, M. A., & Frolking, S. (2018). Tracking vegetation phenology across diverse North American biomes using PhenoCam imagery. *Scientific Data*, 5, 180028. <https://doi.org/10.1038/sdata.2018.28>
- Richardson, A. D., Keenan, T. F., Migliavacca, M., Ryu, Y., Sonnentag, O., & Toomey, M. (2013). Climate change, phenology, and phenological control of vegetation feedbacks to the climate system. *Agricultural and Forest Meteorology*, 169, 156–173. <https://doi.org/10.1016/j.agrformet.2012.09.012>
- Shen, M., Sun, Z., Wang, S., Zhang, G., Kong, W., Chen, A., & Piao, S. (2013). No evidence of continuously advanced green-up dates in the Tibetan plateau over the last decade. *Proceedings of the National Academy of Sciences of the United States of America*, 110(26), E2329. <https://doi.org/10.1073/pnas.1304625110>
- Shen, M., Piao, S., Jeong, S.-J., Zhou, L., Zeng, Z., Ciais, P., Chen, D., Huang, M., Jin, C. S., Li, L. Z. X., Li, Y., Myneni, R. B., Yang, K., Zhang, G., Zhang, Y., & Yao, T. (2015). Evaporative cooling over the Tibetan Plateau induced by vegetation growth. *Proceedings of the National Academy of Sciences of the United States of America*, 112(30), 9299–9304. <https://doi.org/10.1073/pnas.1504418112>
- Tan, B., Morisette, J., Wolfe, R., Gao, F., Ederer, G., Nightingale, J., & Pedelty, J. (2011). An enhanced TIMESAT algorithm for estimating vegetation phenology metrics from MODIS data. *IEEE Journal of Selected Topics in Applied Earth Observations and Remote Sensing*, 4(2), 361–371. <https://doi.org/10.1109/JSTARS.2010.2075916>
- Tian, F., Cai, Z., Jin, H., Hufkens, K., Scheifinger, H., Tagesson, T., Smets, B., van Hoolst, R., Bonte, K., Ivits, E., Tong, X., Ardö, J., & Eklundh, L. (2021). Calibrating vegetation phenology from Sentinel-2 using eddy covariance, PhenoCam, and PEP725 networks across Europe. *Remote Sensing of Environment*, 260(March), 112456. <https://doi.org/10.1016/j.rse.2021.112456>
- Torre Cerro, R., & Holloway, P. (2021). A review of the methods for studying biotic interactions in phenological analyses. *Methods in Ecology and Evolution*, 12(2), 227–244. <https://doi.org/10.1111/2041-210X.13519>
- Van Niel, T. G., & McVicar, T. R. (2004). Determining temporal windows for crop discrimination with remote sensing: A case study in South-Eastern Australia. *Computers and Electronics in Agriculture*, 45(1–3), 91–108. <https://doi.org/10.1016/j.compag.2004.06.003>
- Verhoef, W. (1996). *Application of harmonic analysis of NDVI time series (HANTS). Fourier analysis of temporal NDVI in the Southern African and American continents* (Vol. 108). DLO Winand Staring Centre.
- Vreugdenhil, M., Navacchi, C., Bauer-Marschallinger, B., Hahn, S., Steele-Dunne, S., Pfeil, I., Dorigo, W., & Wagner, W. (2020). Sentinel-1 cross ratio and vegetation optical depth: A comparison over Europe. *Remote Sensing*, 12(20), 3404. <https://doi.org/10.3390/rs12203404>
- Vreugdenhil, M., Wagner, W., Bauer-Marschallinger, B., Pfeil, I., Teubner, I., Rüdiger, C., & Strauss, P. (2018). Sensitivity of Sentinel-1 backscatter to vegetation dynamics: An Austrian case study. *Remote Sensing*, 10(9), 1396. <https://doi.org/10.3390/rs10091396>
- Wang, C., Bond-Lamberty, B., & Gower, S. T. (2003). Carbon distribution of a well- and poorly-drained black spruce fire chronosequence. *Global Change Biology*, 9(7), 1066–1079. <https://doi.org/10.1046/j.1365-2486.2003.00645.x>
- Whitcraft, A. K., Becker-Reshef, I., Justice, C. O., Gifford, L., Kavvada, A., & Jarvis, I. (2019). No pixel left behind: Toward integrating Earth Observations for agriculture into the United Nations Sustainable Development Goals framework. *Remote Sensing of Environment*, 235, 111470. <https://doi.org/10.1016/j.rse.2019.111470>
- Wilson, A. M., & Jetz, W. (2016). Remotely sensed high-resolution global cloud dynamics for predicting ecosystem and biodiversity distributions. *PLoS Biology*, 14(3), e1002415. <https://doi.org/10.1371/journal.pbio.1002415>
- Xiao, X., Braswell, B., Zhang, Q., Boles, S., Frolking, S., & Moore, B. (2003). Sensitivity of vegetation indices to atmospheric aerosols: Continental-scale observations in Northern Asia. *Remote Sensing of Environment*, 84(3), 385–392. [https://doi.org/10.1016/S0034-4257\(02\)00129-3](https://doi.org/10.1016/S0034-4257(02)00129-3)
- Yang, G., Shen, H., Zhang, L., He, Z., & Li, X. (2015). A moving weighted harmonic analysis method for reconstructing high-quality SPOT VEGETATION NDVI time-series data. *IEEE Transactions on Geoscience and Remote Sensing*, 53(11), 6008–6021. <https://doi.org/10.1109/TGRS.2015.2431315>
- Zhang, L., Hickel, K., Dawes, W. R., Chiew, F. H. S., Western, A. W., & Briggs, P. R. (2004). A rational function approach for estimating mean annual evapotranspiration. *Water Resources Research*, 40(2), W02502. <https://doi.org/10.1029/2003WR002710>
- Zhang, Q., Kong, D., Shi, P., Singh, V. P., & Sun, P. (2018). Vegetation phenology on the Qinghai-Tibetan Plateau and its response to climate change (1982–2013). *Agricultural and Forest Meteorology*, 248, 408–417. <https://doi.org/10.1016/j.agrformet.2017.10.026>
- Zhang, X. (2015). Reconstruction of a complete global time series of daily vegetation index trajectory from long-term AVHRR data. *Remote Sensing of Environment*, 156, 457–472. <https://doi.org/10.1016/j.rse.2014.10.012>
- Zhang, X., Friedl, M. A., & Schaaf, C. B. (2006). Global vegetation phenology from Moderate Resolution Imaging Spectroradiometer (MODIS): Evaluation of global patterns and comparison with in situ measurements. *Journal of Geophysical Research: Biogeosciences*, 111(G4), G04017. <https://doi.org/10.1029/2006JG000217>

- Zhang, X., Friedl, M. A., Schaaf, C. B., Strahler, A. H., Hodges, J. C. F., Gao, F., Reed, B. C., & Huete, A. (2003). Monitoring vegetation phenology using MODIS. *Remote Sensing of Environment*, 84(3), 471–475. [https://doi.org/10.1016/S0034-4257\(02\)00135-9](https://doi.org/10.1016/S0034-4257(02)00135-9)
- Zhang, X., Tarpley, D., & Sullivan, J. T. (2007). Diverse responses of vegetation phenology to a warming climate. *Geophysical Research Letters*, 34(19), L19405. <https://doi.org/10.1029/2007GL031447>
- Zhang, Y., Xiao, X., Wu, X., Zhou, S., Zhang, G., Qin, Y., & Dong, J. (2017). A global moderate resolution dataset of gross primary production of vegetation for 2000–2016. *Scientific Data*, 4, 170165. <https://doi.org/10.1038/sdata.2017.165>
- Zhang, Y., Xiao, X., Zhou, S., Ciais, P., McCarthy, H., & Luo, Y. (2016). Canopy and physiological controls of GPP during drought and heat wave. *Geophysical Research Letters*, 43(7), 3325–3333. <https://doi.org/10.1002/2016GL068501>

SUPPORTING INFORMATION

Additional supporting information may be found in the online version of the article at the publisher's website.

How to cite this article: Kong, D., McVicar, T. R., Xiao, M., Zhang, Y., Peña-Arancibia, J. L., Filippa, G., Xie, Y., Gu, X. (2022). *phenofit*: An R package for extracting vegetation phenology from time series remote sensing. *Methods in Ecology and Evolution*, 00, 1–20. <https://doi.org/10.1111/2041-210X.13870>